ARTICLE OPEN

GSK-3 regulates CD4-CD8 cooperation for super-armed CD8+ cytolytic T cells in immunotherapy against tumors

Bastien Moës[1,2,3], Janna Krueger[1,2,3], Chen Liu[1,2,3]✉, Nikhil Ponnoor Anto[1,2,3], Atena Nemati[1,2,3], Mikhael Attias[1,2,3], Alexandra Kazanova[1,2,3], Yunfeng Gao[1,2,3], Linda Castoun-Puckett[1,2,3], Andres Carlos Oroya[1,2,3], Lan Huong Nguyen[1,2,3], Auryane Laure Cabald[1,2,3], Thai Hien Tu[1,2,3]✉ and Christopher E. Rudd[1,2,3,4,5]✉

Although the efficacy of immune checkpoint blockade (ICB) depends on coordinated activity across progenitor and terminal effector CD4⁺ and CD8⁺ T-cell compartments, the cell-intrinsic pathways that enable this cooperation remain incompletely defined. Here, we identify glycogen synthase kinase-3 (GSK-3) as a central regulator of TCF-1⁺ progenitor and memory CD8⁺ T-cell differentiation, where reduced GSK-3 expression enhances antiviral and anti-tumor immunity. In GSK-3 knockdown (GSK-3 KD) mice, diminished GSK-3 reshaped basal T-cell homeostasis, skewing differentiation toward memory-phenotype subsets even in the absence of antigenic stimulation. During chronic LCMV Cl13 infection, GSK-3 KD promoted the expansion and proliferation of GP33-specific memory-precursor effector cells (MPECs). Metabolic profiling by Seahorse and SCENITH revealed increased glycolysis and oxidative phosphorylation in GSK-3 KD TCF-1⁺ stem-like CD8⁺ T cells, with greater GLUT1 expression and mitochondrial mass, indicative of enhanced metabolic adaptability. GSK-3 was also required for regulatory T-cell (Treg) suppressive function, while GSK-3 inhibition and reduced expression synergized with PD-1 blockade to "super-arm" cytolytic CD8⁺ T cells, characterized by upregulation of perforin and seven distinct granzymes. Notably, whereas B16-F10 tumor rejection in wild-type mice relied on CD4⁺ CTLA-4⁺ Tregs, tumor control in GSK-3 KD mice required CD4⁺ T-cell help for optimal granzyme induction and tumor rejection. Together, these findings define a GSK-3–PD-1 signaling axis that links metabolic and differentiation programs to govern T-cell fate and cytotoxicity, providing a mechanistic framework for overcoming ICB resistance.

Signal Transduction and Targeted Therapy (2026)11:188 ; https://doi.org/10.1038/s41392-026-02663-y

INTRODUCTION

The nature and amplitude of the adaptive immune response is controlled by multiple subsets of antigen presenting cells, helper, suppressor and cytolytic T-cells together with effector, memory and exhaustion phases of the response.[1] Further, CD4+ and CD8 + T-cells collaborate to eliminate virally infected cells as well as cancer.[2,3] In this context, CD4 + T-cells can provide help for the development of cytotoxic effector CD8+ responses as well as long-lasting memory.[4–6] Without this support, CD8 + T-cell function is suboptimal and impaired in their control infections and tumor growth.[4,5,7,8] CD4 cells can provide help through various mechanisms, including the production of cytokines such as IL-2, IFN-γ, and TNF-α, and by enhancing dendritic cell function.[6] By contrast, CD4 + FOXP3+ regulatory T-cells (Tregs) maintain immune tolerance while suppressing anti-tumor immune responses.[9] The manipulation of CD4 + T-cell help versus Treg activity has proven a promising strategy for cancer immunotherapy.[10,11]

The repeated antigen-receptor (TCR) engagement and the continuous long-term exposure to antigen can cause a dysfunction or exhaustion which impairs the clearance of pathogens and tumors.[12–14] Inhibitory co-receptors such as cytotoxic T-lymphocyte antigen 4 (CTLA-4), programmed death-1 (PD-1), and lymphocyte-activation gene 3 (LAG-3) act as key functional markers of exhaustion.[15] Within this grouping, the transcription factor, T cell factor 1 (TCF-1) defines early progenitor stem-like exhausted T cells while other markers like TIM-3, CX3CR1 and CD101 define transitory or terminally exhausted stages.[16–19] In this context, immune checkpoint blockade (ICB) has revolutionized cancer treatment.[20,21] This is mediated by antibodies that block the ability of inhibitory receptors to engage their ligands,[20,22–24] while also inducing internalisation.[25] TCF-1+ progenitor stem-like memory T-cells are essential for successful ICB,[26–28] as are effector cytolytic T-cells (CTLs) that release cytotoxic granules containing perforin and granzymes (GZMs) needed to induce apoptosis in target cells.[29,30] Although granzyme B (GZMB) is the best studied GZM, 9 other GZMs are expressed in mice that act on overlapping and unique protein substrates.[31,32]

Receptor-induced intracellular signaling is fundamental to T-cell activation and to the differentiation programs that underpin effective anti-tumor immunity.[33,34] These signaling events are orchestrated by coordinated actions of protein-tyrosine, serine/threonine, and lipid kinases, together with GTP-binding proteins and their downstream effectors.[34–37] We previously demonstrated that the protein-tyrosine kinase p56^{lck} associates with the CD4 or

[1]Department of Medicine, Université de Montréal, Montréal, QC, Canada; [2]Département de microbiologie, infectiologie et immunologie, Université de Montréal, Montreal, QC, Canada; [3]Cell Signaling and Immunotherapy Section, Research Center Hopital Maisonneuve-Rosemont (CR-HMR) Montreal, Montreal, QC, Canada; [4]Division of Endocrinology and Metabolism, Department of Medicine, McGill University, Montreal, QC, Canada and [5]University Institute for Hematology-Oncology and Cell Therapy, Hopital Maisonneuve-Rosemont, Montreal, QC, Canada
Correspondence: Chen Liu (chen.liu@umontreal.ca) or Thai Hien Tu (thai.hien.tu@umontreal.ca) or Christopher E Rudd (christopher.e.rudd@umontreal.ca)

Received: 8 May 2025 Accepted: 2 March 2026
Published online: 20 May 2026

© The Author(s) 2026

CD8 co-receptors to initiate the T-cell receptor (TCR)–dependent signaling cascade.[33,38,39] Activated p56^{lck} phosphorylates immunoreceptor tyrosine-based activation motifs (ITAMs) within the CD3 and ζ chains of the TCR complex[33,38] thereby promoting recruitment and activation of the ζ-chain–associated protein kinase ZAP-70.[40] Acting in concert, Lck and ZAP-70 phosphorylate key adaptor proteins and downstream enzymes, ultimately enabling transcription factor nuclear translocation and the induction of gene expression programs required for T-cell function.[41]

In contrast to p56^{lck} and ZAP-70, which are activated following T-cell receptor engagement to initiate phosphorylation cascades that propagate activating signals, glycogen synthase kinase-3 (GSK-3) functions as a constitutively active serine/threonine kinase in quiescent T cells, where it imposes a tonic inhibitory constraint on activation programs.[42,43] Upon receptor ligation, GSK-3 is rapidly inactivated through upstream signaling pathways, thereby relieving this inhibitory checkpoint and permitting full transcriptional and metabolic reprogramming of activated T cells.[42,43] In mammals, two isoforms of GSK-3 have been identified- a 51 kDa GSK-3α isoform and a 47 kDa GSK-3β isoform which are encoded by separate genes.[43] The phosphorylation of specific serine residues (Ser9: GSK-3β, Ser21: GSK-3α) inactivate the kinase.[44,45] By contrast, phosphorylation at Tyr216: GSK-3β, Tyr279: GSK-3α enhances activity.[46,47] Both isoforms are expressed in numerous tissues[43] and regulate diverse processes.[46,48] Their expression in T-cells inhibits activation and NFAT nuclear occupancy,[49] while the use of broadly-acting inhibitors in a somatostatin–SSTR3–GSK3 signaling setting has been associated with T-cell memory.[50] It has also been reported to promote NK maturation and function.[51] Specific regulatory targets of GSK-3 include the inhibition of glycogen synthase,[52] the regulation of β-catenin expression[53–55] as well as T-cell motility.[56] We have also shown that GSK-3 inactivation can downregulate the transcription and expression of inhibitory co-receptors PD-1 and LAG-3[42,57] and in the process, limit tumor growth.[42,56–61] In this regard, GSK-3 inhibitors have now been approved to treat certain cancers.[62,63]

While immune checkpoint blockade has revolutionized cancer treatment, the key T-cell signaling pathways responsible for its potency remain unclear. Further, the signaling mechanisms that are responsible for CD4-CD8 cooperation in checkpoint blockade therapy are unclear. Here, we show that GSK-3 controls CD4-CD8 T-cell cooperation which operates in synergy with anti-PD-1 to generate super-armed CD8+ effectors in immunotherapy. The genetic downregulation of GSK-3 promoted the presence of TCF-1+ progenitor and memory CD8+ TILs (tumor infiltrating lymphocytes) while inhibiting the suppressor function of Tregs. Further, GSK-3 downregulation, combined with anti-PD-1, unlocked a marked cytotoxic potential in CD8 + T-cells, enabling the expression of a 7 out of 9 granzymes from the mouse genome, a phenomenon not before observed. GSK-3 loss also heightened CD8$^+$ dependence on CD4$^+$ help for optimal granzyme expression and tumor control. These findings define a GSK-3/PD-1 axis linking T-cell fate and metabolism to improved immunotherapy response.

RESULTS

GSK-3 KD mice show increased T-cell memory

To more fully define the role of GSK-3 in T-cell immunity, we generated mice with markedly reduced levels of GSK-3α and GSK-3β in mature T cells (referred to GSK-3 KD mice). This was achieved by crossing mice carrying the distal promoter lck-Cre (dlck-Cre) with mice carrying floxed alleles for *gsk-3α* (gsk-3αflox/flox) and *gsk-3β* (gsk-3βflox/flox). The distal lck promoter drives Cre recombinase expression in peripheral T cells, allowing for gene deletion specifically in mature T cells after their development in the thymus.[64] Immunoblotting with an anti-GSK-3α/β antibody showed a reduced expression of both the GSK-3α and GSK-3β isoforms in splenic CD8+ and CD4 + T cells (Fig. 1a). Although the expression of both isoforms was reduced, the GSK-3β isoform expression was completely lost, while the expression of the GSK-3α isoform was partially reduced.

Initially, we examined the differentiation status of peripheral CD4$^+$ and CD8$^+$ T cells in naïve, unchallenged mice (Supplementary Fig. 1). T-cells from mesenteric lymph nodes (LNs) and spleen of mice born and raised in sterile cages were gated on CD4+ and CD8+ markers (Supplementary Fig. 1a, b, respectively). GSK-3 KD mice displayed a marked reduction in naïve T cells (CD44$^-$CD62L$^+$), particularly within the CD8$^+$ compartment. In contrast, both CD4$^+$ and CD8$^+$ T cells from GSK-3 KD mice exhibited increased frequencies of central memory (T_{CM}; CD44$^+$CD62L$^+$) and effector memory (T_{EM}; CD44$^+$CD62L$^-$/lo) subsets. This shift was compartment-specific, with lymph nodes demonstrating a more pronounced expansion of CD8$^+$ T_{EM} cells, whereas spleens showed a greater increase in T_{CM} cells. Together, these findings identify GSK-3 as a key homeostatic regulator of T-cell fate decisions, constraining memory differentiation and maintaining the naïve pool.

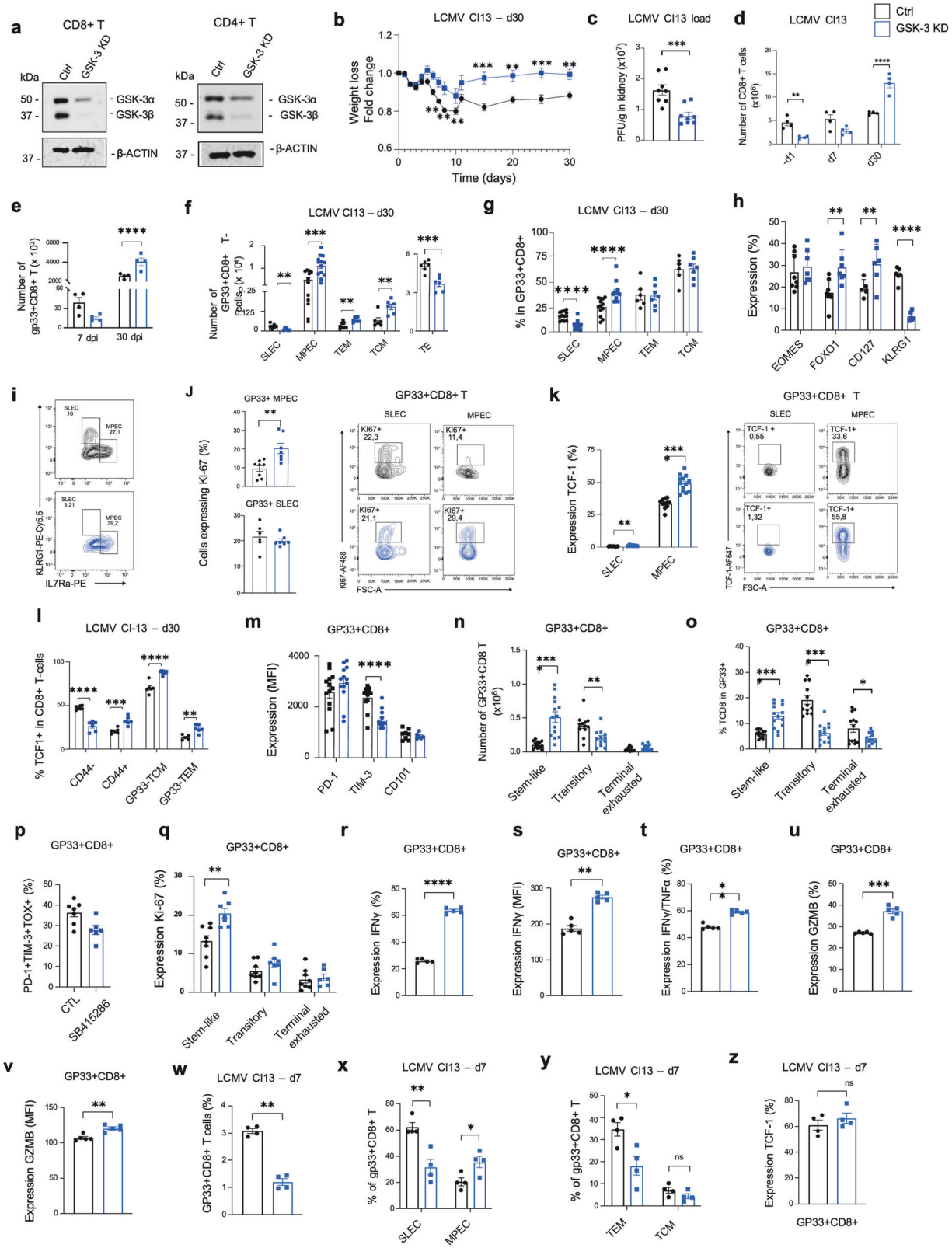
Given this, we next infected mice with Lymphocytic choriomeningitis virus Clone 13 (LCMV Cl13), a prototypic model for chronic viral infection (Fig. 1) (see Materials and Methods), as described.[42,65] Both cohorts showed an initial reduction in body weight; however, GSK-3 KD mice recovered more rapidly, with significantly greater body weight by day 10–30 (Fig. 1b). Correspondingly, LCMV Cl-13 viral titres were lower in GSK-3 KD mice compared to WT mice (Fig. 1c). In contrast, no differences in weight were observed with acute LCMV Armstrong infection at either day 7 (Supplementary Fig. 2a), or day 30 (Supplementary Fig. 2b).

Temporal analysis revealed a shift in cellular dynamics where although splenic GSK-3 KD T cell levels started at a lower level, they surpassed WT mice numbers during late-stage infection (Fig. 1d). Specifically, GSK-3 KD CD8$^+$ T-cell numbers were lower when measured one day before infection (i.e., day −1) and at day 7 of infection, a pronounced expansion was evident during the chronic phase of infection at day 30, with a two-fold increase compared with WT controls. Consistent with this, GP33-specific CD8$^+$ T cells, identified using an H-2D^b–KAVYNFATM–BV421 tetramer, were also significantly more abundant in GSK-3 KD mice at day 30 (Fig. 1e). Together, these findings indicate that reduced GSK-3 expression promotes enhanced expansion and/or persistence of virus-specific CD8$^+$ T cells under conditions that typically favor T-cell exhaustion.

To investigate the cellular mechanisms underlying this effect, we next examined the differentiation status of the CD8$^+$ T-cell compartment. GSK-3 KD mice exhibited increased numbers of GP33 tetramer–positive CD8$^+$ memory-precursor effector cells (MPECs; CD8$^+$KLRG1$^-$CD127$^+$) (Fig. 1f). The number of MPECs increased from a mean of 0.5×10^6 in WT mice to 1.4×10^6 in GSK-3 KD mice. By contrast, the number of short-lived effector cells (SLECs; CD8$^+$KLRG1$^+$CD127$^-$) was reduced. The number of GP33$^+$CD8$^+$ terminal effector T cells was also reduced in GSK-3 KD mice as defined by CD8 + KLRG1$^+$CD39$^+$CD127$^-$ CD44$^+$CD62L$^-$TCF-1$^-$GZMB$^+$ (Fig. 1f) or by CD8$^+$ KLRG1$^+$ CD127$^-$ CD44$^+$ CD62L$^-$ TCF-1-GZMB$^+$ (Supplementary Fig. 2c). KLRG1$^+$ is a marker for effector CD8$^+$ T cells and is lost in memory T-cells.[66,67]

An increase in the GSK-3 KD MPEC population and reduction in SLECs was also evident when expressed as a percentage of GP33-specific CD8$^+$ T cells (Fig. 1g). These data showed that in the context of LCMV Cl13 infection, GSK-3 KD skews CD8$^+$ responses toward a memory-precursor and long-lived memory phenotype at the expense of terminal effector differentiation.

In parallel, we observed elevated expression of FOXO1$^+$ and CD127$^+$ (i.e., IL-7R) CD8$^+$ cells, accompanied by a marked reduction in KLRG1-expressing CD8$^+$ T cells (Fig. 1h). Eomesodermin (EOMES) expression remained unchanged. CD127 is a



canonical marker of memory-precursor and memory CD8⁺ T cells, while the transcription factor FOXO1 is essential for memory establishment, sustaining TCF-1 and IL-7Rα expression, while repressing terminal effector programs such as T-bet.[68] Although EOMES contributes to both effector and memory traits, it typically remains stable during late memory differentiation. A representative FACS profile demonstrated increased CD127 and reduced KLRG1 expression, confirming the expansion of MPECs in GSK-3 KD mice (Fig. 1l).

Consistent with this, Ki-67 expression, a marker for cell division,[69] increased selectively in the GSK-3 KD CD8+ GP33+ MPEC population (Fig. 1j, left panel). While 9.7% of GP33-

Fig. 1 GSK-3 knockdown regulates CD8⁺ T-cell progenitor maintenance and limits exhaustion during chronic viral infection. **a** Immunoblot analysis of GSK-3α and GSK-3β protein expression in splenic CD4⁺ and CD8⁺ T cells isolated from wild-type (WT) control and GSK-3 KD mice ($n = 3$). **b** Body weight curves following intravenous infection with LCMV Clone 13 (Cl-13; 2×10^6 PFU). GSK-3 KD mice recovered more rapidly and maintained significantly higher body weights from day 10 onwards ($n = 14$ per group; data pooled from three independent experiments). **c** Splenic LCMV Cl13 viral titres measured by plaque assay in kidney homogenates from WT and GSK-3 KD mice at day 30 p.i. ($n = 7$–8). **d** Absolute counts of splenic CD8⁺ T cells in LCMV Cl13-infected mice at days −1, 7, and 30 p.i. ($n = 4$). **e** Number of GP33-specific (H-2D^b–KAVYNFATM–BV421 tetramer-positive) CD8⁺ T cells in the spleen at days 7 and 30 p.i. ($n = 4$). **f** Absolute numbers of GP33⁺CD8⁺ memory-precursor effector cells (MPECs; KLRG1⁻CD127⁺), short-lived effector cells (SLECs; KLRG1⁺CD127⁻), effector memory (TEM; CD44⁺CD62L⁻), central memory (TCM; CD44⁺CD62L⁺), and terminal effector (TE) cells in the spleen at day 30 p.i. ($n = 6$–8; data pooled from two independent experiments). GSK-3 KD mice exhibited significantly expanded MPEC, TEM, and TCM populations relative to WT controls. **g** Frequencies of MPECs, SLECs, TEM, and TCM as a percentage of GP33⁺CD8⁺ splenic T cells at day 30 p.i. ($n = 6$–16; data pooled from three independent experiments). **h** Percentage of GP33⁺CD8⁺ T cells expressing EOMES, FOXO1, CD127 (IL-7Rα), or KLRG1 at day 30 p.i. ($n = 5$–8). GSK-3 KD CD8⁺ T cells exhibited elevated FOXO1 and CD127 expression and reduced KLRG1 relative to WT counterparts. **i** Representative flow cytometry dot plots showing MPEC (upper panel) and SLEC (lower panel) cells among GP33⁺CD8⁺ T cells at day 30 p.i. (representative of $n = 7$–12; data pooled from two independent experiments). **j** Ki-67 expression in GP33⁺CD8⁺ SLEC and MPEC populations. Left panel: quantification of Ki-67⁺ cells in each subset ($n = 6$–7). Right panel: representative flow cytometry histograms for WT (upper) and GSK-3 KD (lower) cells. Elevated Ki-67 was observed selectively within the GSK-3 KD MPEC population. **K** TCF-1 expression (%) in GP33⁺CD8⁺ SLEC and MPEC subsets. Left panel: percentage of TCF-1⁺ cells among MPECs in WT and GSK-3 KD mice ($n = 7$–12; data pooled from two independent experiments). Right panel: representative flow cytometry profiles. **l** Percentage of TCF-1⁺ cells within CD44⁻, CD44⁺, GP33⁺TCM, and GP33⁺TEMCD8⁺ T-cell subsets at day 30 p.i. ($n = 5$–7; representative of two independent experiments). **m** Expression of exhaustion markers PD-1, TIM-3, and CD101 on GP33⁺CD8⁺ T cells at day 30 p.i. ($n = 12$–14; data pooled from two independent experiments). TIM-3 expression was significantly reduced on GSK-3 KD GP33⁺CD8⁺ T cells. **n** Absolute numbers of progenitor stem-like (TIM-3⁻TCF-1⁺), transitionally exhausted (CX3CR1⁺TIM-3⁺CD101⁻), and terminally exhausted (CX3CR1⁻TIM-3⁺CD101⁺) cells within PD-1⁺GP33⁺CD8⁺ T cells ($n = 12$–14; pooled from ≥2 independent experiments). **o** Corresponding frequencies of the three exhaustion subsets as a percentage of PD-1⁺GP33⁺CD8⁺ T cells ($n = 12$–14; pooled from ≥2 independent experiments). **p** Percentage of PD-1⁺TIM-3⁺TOX⁺ GP33⁺CD8⁺ T cells in spleens of WT mice treated with the GSK-3 inhibitor SB415286. **q** Ki-67 expression across progenitor stem-like, transitional, and terminally exhausted GP33⁺CD8⁺ T-cell subsets in WT and GSK-3 KD mice. Elevated Ki-67 was observed selectively in the TCF-1⁺ progenitor subset of GSK-3 KD mice. **r–s** IFN-γ production in GP33⁺CD8⁺ T cells at day 30 p.i., expressed as frequency (°r) and mean fluorescence intensity (MFI; s) ($n = 5$). **t** Frequency of dual IFN-γ⁺TNF-α⁺ GP33⁺CD8⁺ T cells at day 30 p.i. ($n = 5$). **u–v** Granzyme B (GZMB) expression in GP33⁺CD8⁺ T cells, shown as percentage (°u) and MFI (v) ($n = 5$). **w** Percentage of GP33⁺CD8⁺ T cells in the spleen at day 7 p.i. ($n = 4$). **x** MPEC and SLEC frequencies among GP33⁺CD8⁺ T cells at day 7 p.i. ($n = 5$). **y** T_E^M and T_C^M frequencies among GP33⁺CD8⁺ T cells at day 7 p.i. ($n = 4$). **z** TCF-1 expression (%) in GP33⁺CD8⁺ T cells at day 7 p.i. ($n = 4$). No significant difference in TCF-1 expression was observed at this early timepoint. Data are presented as mean ± s.e.m. Statistical comparisons were performed by unpaired two-tailed Student's t-test. $^*P < 0.05$, $^{**}P < 0.01$, $^{***}P < 0.001$, $^{****}P < 0.0001$; NS not significant

CD8⁺WT cells expressed Ki-67, 21% of GP33-CD8⁺ GSK-3 KD cells expressed the marker. By contrast, the proliferation in the SLEC population was unaffected by the reduced GSK-3 expression. This differential effect on the MPEC cells was also shown in a representative FACs plot (right panel). These results showed increased cell division was induced by the reduction in GSK-3 expression selectively on MPEC GP33-CD8 + T-cells. Taken together, these findings show that GSK-3 downregulation selectively promotes the differentiation of memory-precursor CD8⁺ T cells early during infection, biasing the response toward a durable memory fate. Under physiological conditions, GSK-3 expression would therefore normally act as a negative regulator of CD8⁺ T-cell persistence, instead, promoting terminal effector differentiation while restraining the formation of long-lived memory precursors.

As a further control, acute infection with the LCMV Armstrong strain also increased T_{EM} cells in GSK-3 KD mice relative to wild-type (WT) mice at day 7 (Supplementary Fig. 2a, right panel). By day 30, consistent with a contraction/memory phase, the same Armstrong strain infection showed a relative shift toward an increase in T_{CM} GP33-CD8 T-cells compared to T_{EM} cells (Supplementary Fig. 2b right panel). There were also fewer GSK-3 KD TE cells upon LCMV Cl-13 infection when compared to WT mice (Supplementary Fig. 2c). In addition, we observed an increase in the percentage of CD44⁺CD4⁺ T cells at day 30 post-LCMV cl-13 infection and in the absolute numbers of CD4+ and CD44⁺CD4⁺ T cells (Supplementary Fig. 2d). By contrast, while the percentage of Th1, Tfh, and Treg subsets were similar in the spleen of GSK-3 KD and WT mice, a clear increase in the number of these cells was seen in the spleen of GSK-3 KD mice (Supplementary Fig. 2e). Similarly, the percentage and numbers of B-cells and CD44 + B-cells were indirectly enhanced, as were the frequency and absolute number of germinal-center (CD19⁺CXCR5⁺BCL6⁺) B cells (Supplementary Fig. 2e). These findings indicate that GSK-3 downregulation augments both CD4⁺ T-cell activation and germinal-center B-cell responses without altering the proportional balance among helper T-cell subsets.

GSK-3 KD promotes TCF-1 expression in CD8 + T-cells

Importantly, and central to this paper, within these subsets, GSK-3 KD mice also consistently showed an increased expression of the progenitor stem-like transcription factor TCF-1 in multiple CD8⁺ subsets. The increase in TCF-1 expression in GSK-3 KD was seen in both the SLEC and MPEC cells, but was at its highest level in the MPEC population (i.e., 28% in WT to 56% in GSK-3 KD T cell) (Fig. 1k, left panel). A representative FACs plot of GP33 + CD8 + T-cells showed the same pattern (i.e., 33.6% in WT to 55.8% for GSK-3 KD) (right panel).

Further, there was an increase in the percentage of TCF-1⁺ cells in the CD8⁺CD44+ population and GP33⁺ CD8⁺ CM and EM subsets in GSK-3 KD mice (Fig. 1l). These findings showed that GSK-3 KD promotes the expanded presence of the progenitor marker in a range of CD8⁺ subsets at day 30 of chronic LCMV Cl-13 infection.

GSK-3 KD CD8 + T-cells show reduced exhaustion

We next examined whether reduced GSK-3 expression affected T-cell exhaustion. While the MFI of PD-1 expression was similar on T cells of both genotypes, TIM-3 expression was significantly reduced on GSK-3 KD GP33⁺ CD8⁺ T cells relative to the WT equivalents (Fig. 1m). In this context, PD1 and TIM-3 expression can mark exhausted CD8 + T-cells with reduced effector functions.[70,71] In keeping with this, we also observed an increase in the number of progenitor stem-like TCF-1⁺ GP33⁺ CD8⁺ T cells (i.e., lacking TIM-3) (Fig. 1n). The number of transitory exhausted (PD-1⁺TIM-3⁺CX3CR1⁺) was reduced while terminally exhausted (PD-1⁺TIM-3⁺CX3CR1-CD101⁺) cells were expressed at low levels. Similarly, we observed an increase in percentage of stem-like TCF-1⁺ progenitors accompanied by a decrease in transitory and terminally exhausted cells (Fig. 1o). On average, the presence of

$GP33^+$ $CD8^+$ $PD1^+$ TIM1- cells increased from 7 percent in the WT spleen to 16 percent in the GSK-3 KD mice. Using the GSK-3 inhibitor SB415286, we also noted a decrease in PD-1^+TIM-$3^+$$TOX^+$ exhausted cells in the $GP33^+$ $CD8^+$ population from infected mice (Fig. 1p). Importantly, we also saw an increase in Ki-67 expression preferentially in the $GP33^+$ $CD4^+$ TCF-1+ progenitor stem-like subset (Fig. 1q). Representative FACS profiles of GSK-3 KD versus WT $GP33^+CD8^+PD\text{-}1^+$ splenic T cells also showed an increase in the frequency of TCF-1^+TIM-3^- T cells (i.e., from 12.7 to 39.3%) as well as a decrease in the presence of transitional $CX3CR1^+$ and terminally exhausted $CD101^+$ T cells (Supplementary Fig. 3).

Consistent with reduced exhaustion, the GSK-3 KD $GP33^+CD8^+$ T-cells involving a major loss of GSK-3β and a partial reduction in GSK-3α expression showed a an increase in the frequency (Fig. 1r), and the MFI of IFN-γ production (Fig. 1s). The frequency of IFN-γ^+ $GP33^+$ CD8 + T-cells at day 30 of infection increased from 24 to 82% indicating that the reduction in GSK-3 reversed T-cell exhaustion. There was also a higher percentage of dual IFN-γ^+ x TNF-α^+ cells (Fig. 1t). Granzyme B expression was likewise elevated in both the percentage and MFI among $GP33^+CD8^+$ T cells (Fig. 1u, v), indicating reinforced cytotoxic potential. Together, these data demonstrate that partially-reduced GSK-3 expression preserves effector competence and cytokine polyfunctionality under chronic antigen exposure. Moreover, using a moderate genetic knockdown model, we show that GSK-3 constrains the generation of TCF-1^+ stem-like progenitors, thereby limiting exhaustion and sustaining functional GP33-specific $CD8^+$ T-cell responses at day 30.

As a control, we examined GSK-3 KD T cells at an earlier timepoint (day 7 post-infection). At this stage, GSK-3 KD mice displayed a reduced frequency of T cells (Fig. 1w), accompanied by an increase in MPECs and a reduction in SLECs (Fig. 1x). While there was a decrease in T_{EM} cells at day 7 (Fig. 1y), no increase in TCF-1 expression was yet observed (Fig. 1z). This early skewing toward an MPEC fate—coupled with the later expansion of TCF1+ progenitors by day 30—suggests that reduced GSK-3 expression initiates an intrinsic differentiation trajectory that favors progenitor maintenance and limits terminal exhaustion, ultimately supporting durable antiviral immunity.

GSK-3 acts as a metabolic gatekeeper of T cells

The increased frequency of TCF-1^+ T cells in GSK-3 KD mice suggested that GSK-3 may regulate the activation threshold of T cells in response to TCR engagement. To assess proliferative responses, splenic T cells were labeled with Tag-it Violet™ (a proliferation-tracking dye) and stimulated in vitro with graded concentrations of soluble anti-CD3 (0.005–2 μg ml^{-1}) for 72 h (Fig. 2a). Flow-cytometric analysis was then performed on gated $CD4^+$ and $CD8^+$ T-cell populations. Both WT and GSK-3 KD T cells exhibited an array of distinct division peaks corresponding to successive rounds of proliferation across the 0.01–2.0 μg ml^{-1} anti-CD3 range. However, at the lowest concentration (0.005 μg/ml), GSK-3 KD T cells showed three distinct division peaks relative to unstimulated controls ($n = 8$, arrows). This contrasted with WT $CD8^+$ T cells which displayed a single division peak with only a faint indication of a second. A similar effect was observed in CD4 and CD8 + T-cells where GSK-3 KD cells showed a greater number of cell divisions at the lower and higher anti-CD3 concentrations (Supplementary Fig. 4). In some experiments, GSK-3 KD T-cells were seen to proliferate at concentrations as low as a remarkable 0.0025 ug/ml. These observations indicate that GSK-3 down-regulation confers heightened proliferative competence, allowing T cells to undergo successive divisions even under sub-optimal TCR stimulation.

A similar trend was observed when monitoring the marker of cellular proliferation, Ki-67 (Fig. 2b). Following low-dose anti-CD3 stimulation (0.005 μg/ml), approximately 70% of GSK-3 KD T-cells expressed Ki-67 compared to 30% of WT cells. A more modest but still significant increase was also detected at higher anti-CD3 concentrations, indicating that reduced GSK-3 expression enhances proliferation across a range of activation thresholds. A comparable effect on both $CD4^+$ and $CD8^+$ T-cells was confirmed in independent experiments as anti-CD3 concentrations as low as 0.0025ug/ml (Supplementary Figs. 5a, b), whereas no consistent difference was observed in the frequency of apoptotic cells or in Bcl-2 expression (Supplementary Fig. 6a–bn). GSK-3 KD $CD4^+$ and $CD8^+$ T-cells also exhibited increased β-CATENIN expression (Supplementary Figs. 6d) with only marginal effects on AKT phosphorylation (Supplementary Fig. 6c).

In this context, metabolism plays key role in T-cell activation.[72–75] Upon activation, T-cells undergo a metabolic switch from oxidative phosphorylation (OXPHOS) to glycolysis.[72–75] The role of GSK-3 in regulating T-cell metabolism has not been fully explored. To assess this, we first measured the oxygen consumption rate (OCR) and extracellular acidification rate (ECAR) in resting and anti-CD3–stimulated T cells after 24 h using a Seahorse XF24 Extracellular Flux Analyzer (Fig. 2c–l). Cells were sequentially treated with mitochondrial perturbing agents, including oligomycin (to inhibit ATP synthase), FCCP (to uncouple the electron transport chain), and rotenone plus antimycin A (to inhibit complexes I and III, respectively).

ECAR, a proxy for glycolytic activity, was measured in a representative experiment (Fig. 2c). Anti-CD3 activated GSK-3 KD T cells exhibited significantly higher basal ECAR levels compared to WT controls, a disparity that was further amplified following the addition of glucose. To assess maximal glycolytic capacity, we administered oligomycin to inhibit mitochondrial ATP synthase. This shift toward compensatory glycolysis further widened the gap, highlighting a robust glycolytic program in GSK-3 KD T cells.

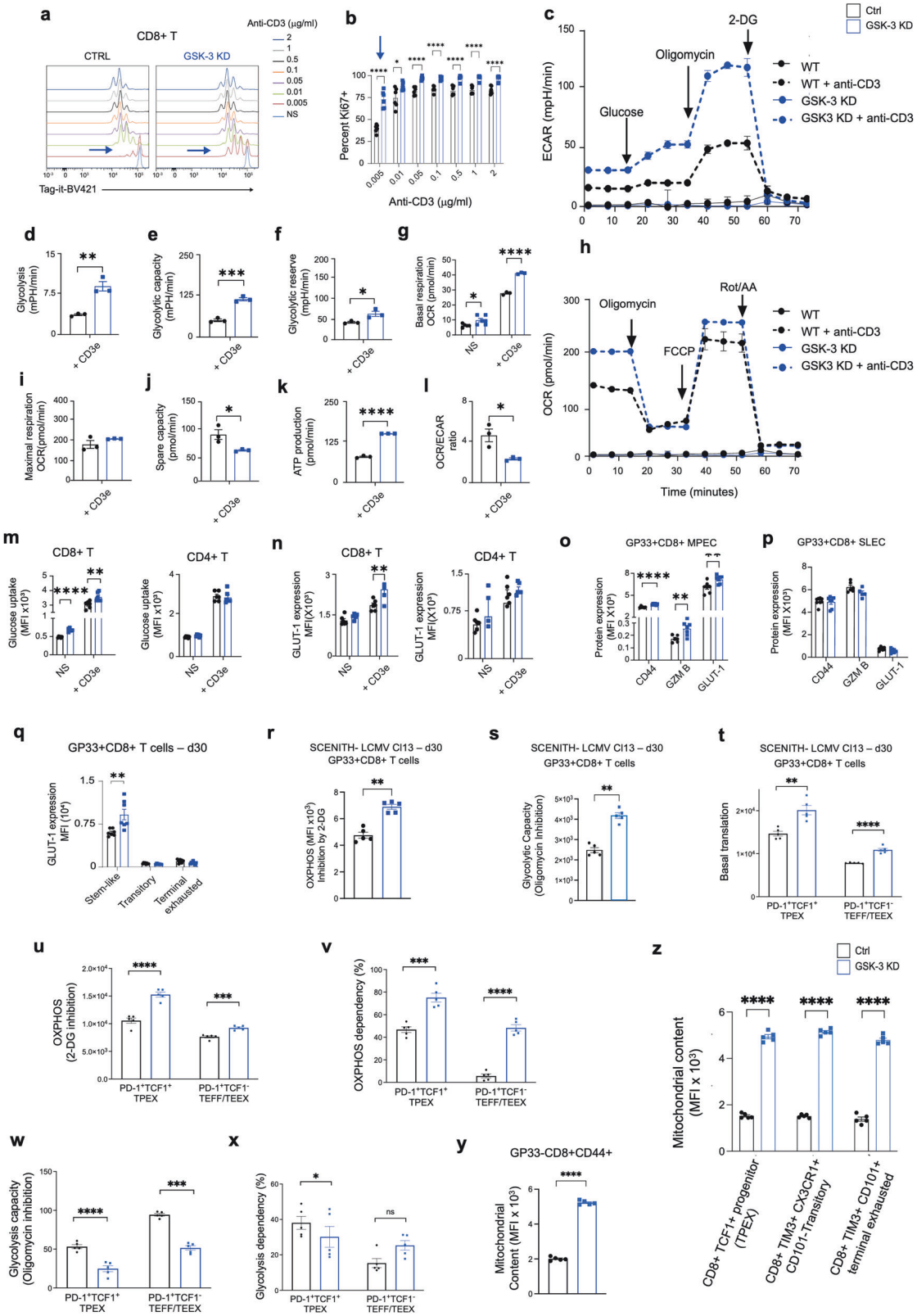
Pooled data from multiple experiments confirmed the enhancement of glycolysis in the GSK-3 KD T-cells (Fig. 2d). Moreover, the same cells exhibited higher glycolytic capacity (Fig. 2e) and an elevated glycolytic reserve, defined as the difference between maximal ECAR after glucose + oligomycin and after glucose alone (Fig. 2f). Collectively, these data suggest that the loss of GSK-3 primes T cells for an enhanced metabolic state with enhanced aerobic glycolysis.

Despite this, GSK-3 levels also influenced mitochondrial respiration, as reflected by changes in OCR profiles (Fig. 2g–k). Both basal and anti-CD3–induced OCR levels were higher in GSK-3 KD T cells compared to wild-type controls (Fig. 2g), as was the response to FCCP (Fig. 2h). FCCP reveals the maximal uncoupled respiratory capacity—the highest achievable oxygen consumption rate when mitochondrial activity is disengaged from ATP production—providing an insight into a T-cell's ability to meet elevated energetic demands. The maximal OCR did not differ significantly between groups (Fig. 2i). Notably, the spare respiratory capacity, defined as the difference between maximal and basal OCR, was reduced in anti-CD3–stimulated GSK-3 KD T cells (Fig. 2j). This is in line with the higher basal OCR levels. Further, consistent with these observations, GSK-3 KD T cells exhibited increased ATP production Fig. 2k), but a decreased OCR/ECAR ratio (Fig. 2l). Together, these findings indicate that loss of GSK-3 enhances mitochondrial output while simultaneously biasing T-cell metabolic programming toward glycolysis.

In support of this glycolytic shift, glucose uptake was elevated in $CD8^+$, but not $CD4^+$ T cells from GSK-3 KD mice (Fig. 2m, left and right panels). This was accompanied by increased expression of the glucose transporter GLUT-1 in CD8 + T-cells (Fig. 2n, left panel).

While GSK-3 KD CD4 T cells exhibited a similar upward trend in GLUT-1 expression, it did not reach the same magnitude as their CD8 counterparts (Fig. 2n right panel). GLUT-1 plays a crucial role in mediating glucose uptake in activated T-cells.[76–78]

In the context of LCMV Cl-13 infection, it was difficult to extract sufficient numbers of cells to conduct Seahorse analysis. Nevertheless, we found that GSK-3 KD $GP33^+$ $CD44^+$ $CD8^+$ MPECs express



a higher MFI of expression of GLUT1 and GZMB than WT cells, an effect not evident on SLECs (Fig. 2o, p, respectively). Intriguingly, GLUT1 expression was selectively upregulated on GSK-3 KD stem-like progenitor exhausted (TPEX) cells (Fig. 2q) but remained negligible on transitory and terminally exhausted subsets. This profile aligns with the increased frequency of Ki67 TCF1^{+} progenitor cells observed 30 days post-infection (Fig. 1o, q). Overall, our findings indicated that GSK-3 affected both the glycolysis and OXPHOS pathways of cellular metabolism, and in particular, by augmenting glycolysis in progenitor CD8^{+} TCF-1^{+} T-cells.

Fig. 2 GSK-3 acts as a metabolic checkpoint governing bioenergetic reprogramming and mitochondrial fitness in CD8⁺ T cells. **a** Representative flow cytometry histogram of CellTrace™ Violet (Tag-it Violet™)-labelled splenic CD8⁺ T cells from WT (CTRL) and GSK-3 KD mice stimulated with graded concentrations of soluble anti-CD3ε (0.005–2 μg ml⁻¹) for 72 h ($n = 4$). Progressive dilution of dye fluorescence reflects successive cell divisions (arrows). GSK-3 KD CD8⁺ T cells underwent multiple rounds of division at the lowest antibody concentration (0.005 μg ml⁻¹), at which WT cells showed minimal proliferation. **b** Quantification of Ki-67⁺ cells among CD8⁺ T cells stimulated as in a. GSK-3 KD T cells exhibited significantly higher proliferation at the lowest anti-CD3ε concentration tested ($n = 6$; data pooled from two independent experiments). Two-way ANOVA with Šidák correction; $^{*}P < 0.05$, $^{****}P < 0.0001$. **c** Representative extracellular acidification rate (ECAR) traces from splenic T cells activated with anti-CD3ε (1 μg ml⁻¹) for 24 h, with sequential injections of D-glucose, oligomycin, and 2-deoxyglucose (2-DG). Both basal and stimulated glycolytic activity were markedly elevated in GSK-3 KD T cells. **d–f** Quantification of glycolytic parameters: glycolysis (**d**), glycolytic capacity (**e**), and glycolytic reserve (**f**), derived from ECAR traces ($n = 3$). **g** Representative oxygen consumption rate (OCR) traces from T cells activated with anti-CD3ε (1 μg ml⁻¹) for 24 h, with sequential injections of oligomycin, FCCP, and rotenone/antimycin A (Rot/AA). Basal and stimulated OCR values were elevated in GSK-3 KD T cells. **h–k** Quantification of respiratory parameters: OCR in response to FCCP (**h**), maximal respiration (**i**), spare respiratory capacity (**j**), and ATP production rate (k) ($n = 3$). **l** Ratio of maximal OCR to maximal ECAR in activated T cells ($n = 3$). **m–n** Glucose uptake assessed by 2-NBDG incorporation (**m**) and GLUT1 expression by flow cytometry (**n**) in CD8⁺ and CD4⁺ T cells, either unstimulated or activated with anti-CD3ε (1 μg ml⁻¹) for 24 h ($n = 5$–6). Increased glucose uptake and GLUT1 expression were selectively observed in CD8⁺, but not CD4⁺, T cells from GSK-3 KD mice. **o–p** GLUT1, CD44, and GZMB MFI in GP33⁺CD8⁺ MPECs (**o**) and SLECs (**p**) at day 30 p.i. with LCMV Cl13. GLUT1 and GZMB were selectively elevated in GSK-3 KD MPECs. **q** GLUT1 expression (MFI) on progenitor stem-like, transitionally exhausted, and terminally exhausted GP33⁺CD8⁺ T-cell subsets at day 30 p.i. ($n = 5$–7). GLUT1 was predominantly expressed on TCF-1⁺ progenitor cells and was selectively increased in the GSK-3 KD progenitor subset. **r–s** SCENITH analysis of GP33⁺CD8⁺CD44⁺ T cells at day 30 p.i. with LCMV Cl13. **r** shows puromycin incorporation following 2-DG blockade of glycolysis (reflecting OXPHOS compensatory capacity); **s** shows puromycin incorporation following oligomycin blockade of mitochondrial ATP synthase (reflecting glycolytic compensatory capacity) ($n = 5$). **t** SCENITH-based quantification of basal protein synthesis (MFI) in PD-1⁺TCF-1⁺ progenitor-exhausted (TPEX) versus PD-1⁺TCF-1⁻ effector/terminally exhausted (TEFF/TEEX) GP33⁺CD8⁺ T-cell subsets. **u–v** SCENITH analysis of OXPHOS activity (**u**) and OXPHOS dependency (**v**) in TPEX versus TEFF/TEEX subsets at day 30 p.i. **w–x** SCENITH analysis of glycolytic capacity (**w**) and glycolytic dependency (**x**) in TPEX versus TEFF/TEEX subsets at day 30 p.i. GSK-3 KD TPEX cells exhibited reduced glycolytic dependence and enhanced OXPHOS engagement, consistent with a metabolically flexible progenitor phenotype. **y** Mitochondrial content, assessed by MitoSpy™ Green FM staining (MFI), in GP33⁺CD44⁺CD8⁺ T cells from WT and GSK-3 KD mice at day 30 p.i. ($n = 5$). **z** Mitochondrial mass (MitoSpy MFI) stratified by differentiation state: TCF-1⁺ progenitor, TIM-3⁺CX3CR1⁺CD101⁻ transitionally exhausted, and TIM-3⁺CX3CR1⁻CD101⁺ terminally exhausted GP33⁺CD8⁺ T-cell subsets ($n = 5$). Increased mitochondrial content was observed across all differentiation states in GSK-3 KD mice. Data are presented as mean ± s.e.m. unless otherwise stated. Statistical comparisons were performed by unpaired two-tailed Student's t-test unless otherwise stated. $^{*}P < 0.05$, $^{**}P < 0.01$, $^{***}P < 0.001$, $^{****}P < 0.0001$; NS not significant

To complement these findings, we also used SCENITH analysis to profile GP33 + CD8 + T cells at day 30 of infection (Fig. 2r–x). SCENITH is a flow-cytometry–based assay that quantifies cellular dependence on glycolysis versus mitochondrial respiration by measuring changes in protein synthesis following selective metabolic inhibition.[79] Upon glycolysis blockade with 2-DG, GSK-3 KD CD8⁺CD44⁺ T cells maintained significantly higher puromycin incorporation, demonstrating enhanced mitochondrial compensation and greater metabolic flexibility to sustain OXPHOS under conditions of limited glucose flux (Fig. 2r). Conversely, when OXPHOS was inhibited with oligomycin, GSK-3 KD CD8⁺ T cells exhibited a stronger glycolytic compensatory response compared with WT cells (Fig. 2s). This reflects an increased capacity to support ATP production via glycolysis when mitochondrial ATP generation is impaired. Collectively, these in vivo data confirm that the GSK-3 deficiency promotes enhanced engagement of both glycolytic and mitochondrial metabolic programs in CD8⁺ T cells during chronic LCMV Cl13 infection, conferring metabolic flexibility that preserves protein synthesis under metabolic stress.

We also compared these effects with a focus on TCF-1⁺ stem-like T cells. PD-1⁺TCF-1⁺ progenitor (TPEX) cells were compared to the remaining PD-1⁺TCF-1⁻ CD8⁺ T-cell compartment comprising effector (TEFF) and terminally exhausted (TEEX) cells (Fig. 2t–x). GSK-3 KD CD8⁺ T cells exhibited higher basal translation in both the TCF1⁺ TPEX and TCF1⁻TEFF/TEEX subsets compared with WT cells (Fig. 2t). In addition, GSK-3 KD cells maintained elevated OXPHOS during 2-DG-mediated glycolytic inhibition, outperforming WT and effector populations at 30 days post-infection (Fig. 2u). An increase in the percentage dependency on OXPHOS was observed in the GSK-3 KD cells effector and terminally exhausted TEFF/TEEX cells (Fig. 2v). Interestingly, despite their lower basal biosynthetic activity, the TEFF/TEEX CD8⁺ T cells exhibited greater OXPHOS dependence than progenitor-like cells, consistent with a metabolically rigid phenotype.

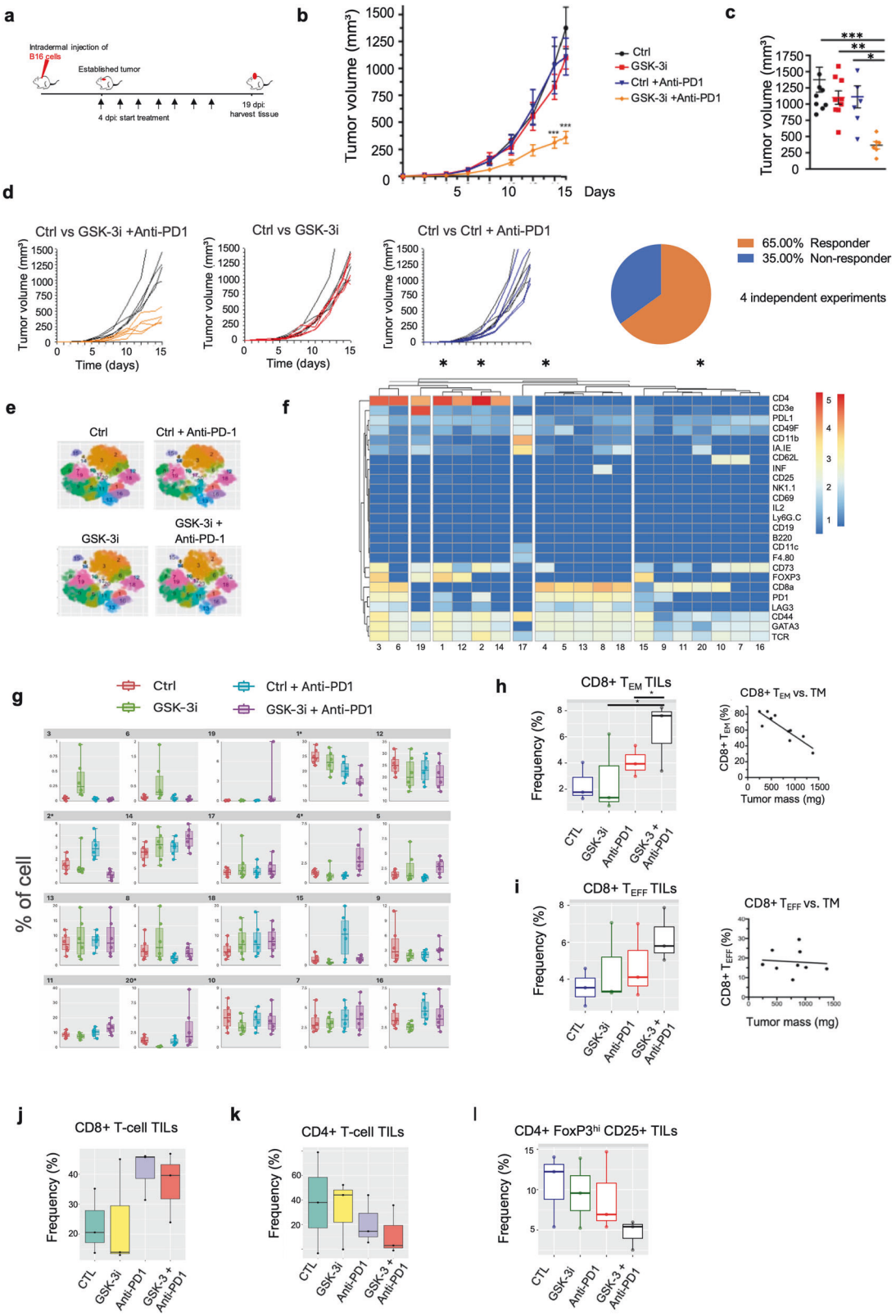
Regarding glycolysis, both GSK-3 KD TPEX and TEFF/TEEX cells exhibited reduced glycolytic capacity compared to WT T cells when OXPHOS was inhibited by oligomycin (Fig. 2w), reflecting a greater reliance on OXPHOS-derived ATP in GSK-3 KD mice. GSK-3 KD TPEX cells also showed slightly lower glycolytic dependence, whereas TEEX cells exhibited a small increase (Fig. 2x). Overall, GSK-3 KD reduces dependence on glycolysis—particularly in TPEX cells—and endows them with balanced metabolic plasticity, allowing efficient engagement of either glycolysis or OXPHOS depending on environmental stress. In contrast, TEFF/TEEX CD8 T-cells from 30-day-old infected mice remain more metabolically constrained, characterized by greater OXPHOS reliance and limited flexibility.

GSK-3 deficiency drives expansion of mitochondrial biomass

Because the concurrent enhancement of glycolysis and OXPHOS suggested a fundamental shift in cellular bioenergetic capacity, we next quantified mitochondrial content in GSK-3–deficient T cells. Using a MitoSpy fluorescent probe, we observed a significant increase in mitochondrial mass within GP33⁺CD44⁺ CD8⁺ T cells from GSK-3 KD mice (Fig. 2y). This increase was evident across multiple differentiation states, including a marked enrichment in TCF-1⁺ progenitor-like CD8⁺ T cells, as well as in TIM-3⁺CX3CR1⁺ transitionally exhausted and surprisingly, in TIM-3⁺CD101⁺ terminally exhausted CD8⁺ T-cells (Fig. 2z). Together, these data indicate that the GSK-3 knockdown promotes increased mitochondrial mass across the CD8⁺ T-cell differentiation stages supporting enhanced energy-generating capacity in progenitor, effector, and exhausted populations. This suggests that GSK-3 acts as a central metabolic brake, and its removal enables a robust mitochondrial program regardless of the T cell's differentiation state.

GSK-3 KD empowers PD-1 blockade to overcome ICB tumor resistance

Given these effects, we next assessed the role of GSK-3 in regulating T-cell responses against tumors (Fig. 3). For this, we derived and used a B16-F10 melanoma subclone (B16-F10 R1) which is resistant to anti-PD-1 treatment. B16-F10 R1 cells were injected intradermally followed by intra-peritoneal injections of



the GSK-3 competitive inhibitor, SB415286 (GSK-3i),[42,57] anti-PD-1 or a SB415286/anti-PD-1 combination, every 4 days (Fig. 3a). The concentrations and properties of the inhibitor and antibody have been previously described[42,58] Neither anti-PD-1 nor SB415286 monotherapy affected tumor growth of this non-immunogenic tumor (Fig. 3b). However, by contrast, the combination of anti-PD-1 and SB415286 synergized to reduce tumor growth from days 8-17 based on tumor volume (Fig. 3b) and tumor weight when measured at day 15 (Fig. 3c). Spider-graphs show reduced volume growth of individual tumors in mice (Fig. 3d, left panels). In

Fig. 3 GSK-3 inhibition synergizes with PD-1 blockade to overcome tumor resistance and remodel the tumor immune microenvironment. **a** Schematic of the experimental design. C57BL/6 WT mice were implanted intradermally with B16-F10 R1 melanoma cells (**a** PD-1-resistant subclone). Mice received intraperitoneal injections of vehicle, SB415286 (GSK-3i), anti-PD-1 antibody, or the combination every 4 days beginning on day 1 post-implantation. **b**,**c** Tumor volume over time (**b**) and tumor weight at day 15 (**c**) for each treatment group ($n = 5$–10; data pooled from ≥2 independent experiments). Combination therapy significantly reduced tumor growth compared to either monotherapy alone. **d** Left panels: spider plots showing the growth trajectory of individual tumors per group. Right panel: pie charts depicting the proportion of responders (defined as ≥50% reduction in tumor volume) in the anti-PD-1 and combination treatment groups (data pooled from four independent experiments). 65% of mice in the combination group responded to therapy. **e** Phenograph visualization of 20 distinct immune cell clusters identified by mass cytometry (CyTOF) in anti-TCRβ-gated tumor-infiltrating lymphocytes (TILs) ($n = 5$–10). **f** Heatmap displaying the relative expression of 15 surface markers across the 20 CyTOF-defined immune clusters. Cluster 20 (★), which expanded significantly with combination therapy, corresponded to a CD8⁺TEM phenotype (CD44⁺CD62L⁻IA-IE⁺PD-L1⁺PD-1⁻LAG-3⁻). Cluster 1 (★), which was diminished, corresponded to immunosuppressive Tregs (CD44⁺CD25⁺FOXP3⁺CD73⁺PD-1⁺LAG-3⁺). **g** Box plots showing the distribution of each immune cluster across treatment groups as a proportion of anti-TCRβ⁺ TILs. **h** Frequency of CD8⁺TEM TILs as a proportion of total TILs (left panel) and correlation with tumor mass (right panel) ($n = 9$). TEM frequency correlated inversely with tumor weight. **i** Frequency of CD8⁺ effector (TEFF) TILs (left) and their correlation with tumor mass (right) ($n = 9$). No significant association between T_E^{ff} frequency and tumor regression was detected. **j** Overall CD8⁺ TIL abundance across treatment groups ($n = 9$). Both anti-PD-1 monotherapy and combination therapy increased total CD8⁺ TIL infiltration. **k**,**l** Frequency of total CD4⁺ TILs (**k**) and CD4⁺FOXP3^{+hi}CD25⁺ T_{AE}^{ψ} (**l**) across treatment groups ($n = 9$). Combination therapy was associated with a marked and significant reduction in intratumoral T_{AE}^{ψ} frequency. Data are presented as mean ± s.e.m. Statistical comparisons were performed by one-way or two-way ANOVA with post-hoc correction. *$P < 0.05$, **$P < 0.01$, ***$P < 0.001$, ****$P < 0.0001$; NS not significant. $n = 3$ independent experiments with 4–5 mice per group

addition, 65% of mice bearing B16-F10 R1 tumors became responsive to combination therapy as opposed to none with monotherapy (right panel). Kaplan-Meier survival analysis demonstrated a survival advantage with combination therapy (Supplementary Fig. 7). Further, the anti-PD-1/SB415286 combination also significantly enhanced tumor control compared to monotherapy in the colorectal MC38 model (Supplementary Fig. 8).

To define the nature of TILs, we used Time-of-Flight (CyTOF) mass cytometry with a panel of 15 monoclonal antibodies (Fig. 3e-m). From this, 20 distinct cellular subsets within the anti-TCRβ positive population became apparent as shown with phenograph illustrations (Fig. 3e), heat maps (Fig. 3f) and boxplot representations (Fig. 3g). Although there were various statistically non-significant upward and downward trends, only two clusters achieved statistical significance (<0.05) (Supplementary Fig. 9). Cluster 20 was expanded and corresponded to a CD8⁺ T-cell subset characterized by the phenotype CD44⁺ CD62L⁻IA-IE⁺CD11b⁻CD73⁻ PD-L1⁺, consistent with a CD8⁺T_{EM} population ($P = 0.013$). Notably, this subset lacked expression of PD-1 and LAG-3, indicating an absence of both transitory and terminal exhaustion phenotypes (Fig. 3f, see asteriks). Conversely, Cluster 1 in the CD4⁺ population was diminished and comprised cells expressing CD44⁺CD25⁺FOXP3⁺ CD73⁺PD-1⁺LAG-3⁺IA-IE⁺CD49f⁺PD-L1⁺, a phenotype characteristic of immunosuppressive regulatory T cells (Tregs) ($P = 0.044$). The reduction of this cluster suggests an attenuated suppressive compartment in GSK-3 KD mice.

Using a less stringent threshold, there was a trend toward reduced frequencies of Cluster 19 CD4⁺ T-cells ($P = 0.09$) (Fig. 3f, see asterisks and Supplementary Fig. 9). This cluster shared many phenotypic markers with the Treg-enriched Cluster 1 but lacked expression of PD-1 and LAG-3, suggesting a less suppressive phenotype. Similarly, the FoxP3⁺ Cluster 12 resembled Cluster 19 but lacked CD49f (integrin α6) and exhibited lower levels of the inhibitory ectoenzyme CD73 ($P = 0.127$). CD73 marks a subset of Tregs with enhanced immunosuppressive capacity.[80,81] Furthermore, CD8+ Cluster 4 showed an increase with a p value of 0.149 resembled Cluster 20, but withexhaustion markers PD-1, LAG3, and CD73. Overall, combination therapy was associated with an increase in CD8⁺ TILs and a decrease in Treg-like CD4⁺ suppressor cells.

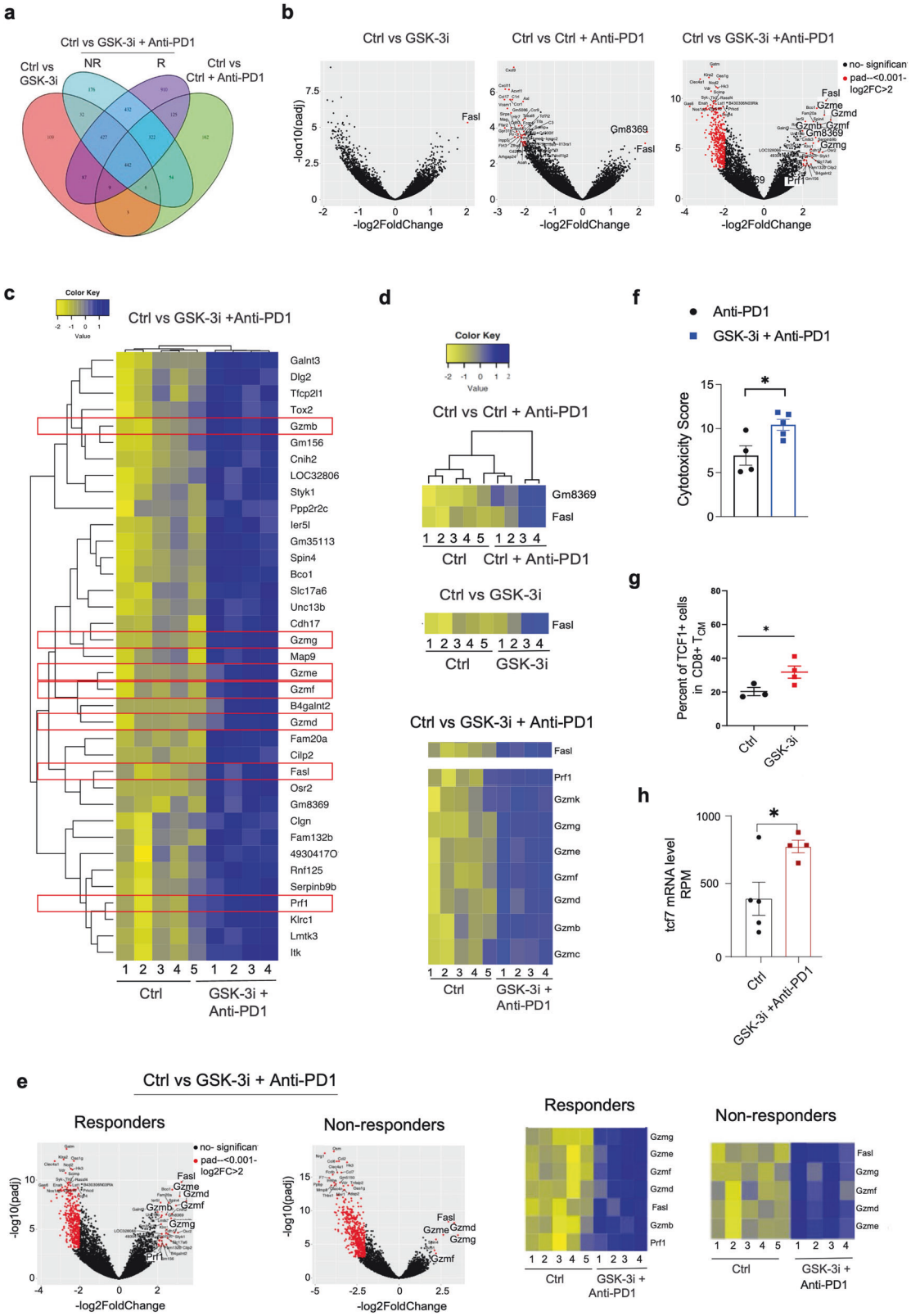
We next employed conventional flow cytometry to validate the CyTOF-based findings (Fig. 3h–l). This complementary analysis confirmed a significant increase in CD8⁺ T_{EM} TILs with combination therapy (Fig. 3h, left panel). Thisfrequency of CD8⁺ T_{EM} cells exhibited a strong inverse correlation with tumor mass (right panel). A similar increase was observed for CD8⁺ effector (T_{EFF}) cells (Fig. 3i, left panel); however, itdid not reach statistical significance and was not associated with tumor regression (right panel). In line with previous reports,[82] anti–PD-1 monotherapy increased CD8⁺ TIL abundance which was unaffected by the presence of SB415286 (Fig. 3j). Together, these data indicate that while PD-1 blockade broadly expands CD8⁺ T-cell infiltration, concomitant GSK-3 inhibition selectively promotes the relative presence of tumor-rejecting cytotoxic CD8⁺ T_{EM} cells.

Conventional flow cytometric analysis also showed a decrease in the presence of CD4⁺ T-cells (Fig. 3k). This effect was most pronounced on suppressor T-cells with a marked reduction in CD4⁺FOXP3^{hi}CD25⁺ Tregs in response to GSK-3i x anti–PD-1 combination therapy (Fig. 3l). FACs staining demonstrated that anti–PD-1 treatment decreased the frequencies of PD-1⁺FOXP3⁺ and TIM-3⁺FOXP3⁺ Tregs (Supplementary Fig. 10), with a modest but reproducible trend to further reduce with combination therapy. Together, these data indicate that GSK-3 inhibition cooperates with PD-1 blockade to constrain immunosuppressive Treg subsets within the tumor microenvironment, thereby favoring a more permissive milieu for effective antitumor immunity

GSK-3KD licenses PD-1 blockade to induce perforin and 7/9 granzymes for enhanced CD8 + CTL TILs

We next assessed the transcriptional programs induced by anti–PD-1 and GSK-3 inhibition, alone or in combination, using bulk RNA-seq analysis of tumor-infiltrating lymphocytes (Fig. 4a–c). Differentially expressed genes were initially defined by a ≥ 2-fold change with $p < 0.01$ relative to untreated controls. A Venn diagram (Fig. 4a) illustrates the distinct and overlapping gene sets modulated by each treatment. Anti–PD-1 monotherapy altered 162 genes, GSK-3i 109 genes, with only three genes shared between the two monotherapies. In contrast, combination therapy elicited a markedly broader transcriptional program, inducing 910 unique genes in tumors from highly responsive mice (defined as >50% tumor reduction relative to untreated controls) and 176 unique genes in non-responders. There was a clear synergy with GSK-3i licensing anti-PD-1 induced alterations in gene expression within T-cells. Network analysis revealed enrichment for genes associated with immune activation and inflammatory response pathways (Supplementary Fig. 11).

To increase analytical stringency, a stricter threshold (≥2-fold change, $p < 0.001$) was applied for a more refined comparison. Volcano profiling showed that the combination of GSK-3i and anti-PD-1 blockade induced a distinct immunogenic signature (Fig. 4b). GSK-3i monotherapy induced the expression of Fasl, encoding the death ligand FasL (left panel). Anti-PD-1 monotherapy mostly downregulated genes included genes involved in immune



adhesion and chemotaxis (*Vcam1*, *Cxcl9*, *Cxcl11*) while upregulating only *Fasl* and *Gm8369* (a predicted non-coding transcript with no currently defined function) (middle panel). By contrast, GSK-3i in combination with anti-PD-1 elicited a robust synergistic transcriptional response, characterized by coordinated up- and down-regulation of gene programs (right panel). A control volcano plot comparing GSK-3i monotherapy to combination therapy is shown in Supplementary Fig. 12. Differential expression analysis revealed induction of cytolytic genes (e.g., Gzmf, Serpinb9b) in the combination treatment relative to GSK-3 alone. GSK-3 inhibition

Fig. 4 Transcriptomic profiling reveals a GSK-3–PD-1 synergistic program driving coordinated granzyme and perforin induction in tumor-infiltrating CD8⁺ T cells. **a** Venn diagram of differentially expressed genes (DEGs) in CD8⁺ TILs isolated from B16-F10 R1 tumors following treatment with anti-PD-1 monotherapy, GSK-3i monotherapy, or combination therapy, relative to untreated controls (≥2-fold change, $P < 0.01$). Anti-PD-1 and GSK-3i monotherapies regulated largely non-overlapping gene sets (162 and 109 DEGs, respectively, with only 3 shared), whereas combination therapy uniquely induced 910 genes in high responders (>50% tumor volume reduction) and 176 genes in non-responders. **b** Volcano plots of DEGs in each treatment group relative to untreated controls, with a stringent threshold (≥2-fold change, $P < 0.001$). GSK-3i monotherapy selectively induced Fasl. Anti-PD-1 monotherapy predominantly downregulated immune adhesion and chemotaxis genes (Vcam1, Cxcl9, Cxcl11). Combination therapy elicited a robust, synergistic transcriptional response dominated by upregulation of cytolytic effector genes. **c** Heatmap of the 37 genes significantly upregulated by combination therapy (stringent threshold). Key upregulated genes include the T-cell signaling kinase Itk, the transcription factor Tox2, perforin (Prf1), and seven of the nine known murine granzymes: Gzmb, Gzmc, Gzmd, Gzme, Gzmf, Gzmg, and Gzmk. **d** Heatmap focusing on cytolytic effector genes comparing expression levels across GSK-3i monotherapy, anti-PD-1 monotherapy, and combination therapy. The coordinated upregulation of perforin and multiple granzymes was exclusively observed with combination treatment. **e** Heatmap of genes upregulated (≥2-fold, $P < 0.001$) in TILs from combination therapy responders versus non-responders. Gzmb, Gzmk, and Prf1 were significantly elevated in responders, underscoring the importance of a broad cytolytic repertoire for effective tumor clearance. **f** Cytotoxicity score computed for each treatment group by averaging normalized expression values of a pre-defined cytolytic gene signature (Gzma, Gzmb, Prf1, Fasl, Ifng, Cd3e, Nkg7, Lgals1, Fgl2, Cxcl11, Nr4a3, Spp1, Icos, Klrg1, Cd8a, and Cd8b1). Combination therapy significantly increased the cytotoxicity score relative to anti-PD-1 monotherapy. Statistical significance assessed by Student's t-test. **g** Quantification of TCF-1⁺ cells within the CD8⁺TCM TIL compartment by flow cytometry ($n = 4$). TCF-1⁺ frequency was elevated following combination therapy. **h** Tcf7 (TCF-1) mRNA expression (reads per million, RPM) in CD8⁺ TILs across treatment groups. Combination therapy was associated with increased Tcf7 transcript levels. Data are presented as mean ± s.e.m. Statistical comparisons were performed by unpaired two-tailed Student's t-test unless otherwise stated. *$P < 0.05$, **$P < 0.01$, ***$P < 0.001$, ****$P < 0.0001$; NS not significant. $n = 3$ independent experiments with 4–5 mice per group

acted as a licensing signal that unlocked the capacity of anti-PD-1 to drive transcriptional changes in TILs.

Genes shown were then further filtered to exclude low-expression transcripts and retain those with consistent expression across samples. Among the 37 genes upregulated by combination therapy versus untreated controls under the more stringent threshold, several were directly linked to T cell activation and effector differentiation, as visualized by heatmap analysis (Fig. 4c). These included interleukin-2–inducible T cell kinase (ITK) and the transcription factor Tox2. ITK is a central mediator of T cell receptor signaling, regulating downstream activation pathways that control cytokine production and lineage commitment,[83] whereas Tox2 supports metabolic adaptation and tissue residency of effector T cells.[84]

However, most strikingly, combination therapy resulted in robust induction of genes for cytolytic machinery, including perforin (*Prf1*) and a remarkable seven of the nine known murine granzymes (*Gzmk, Gzmg, Gzme, Gzmf, Gzmd, Gzmb, and Gzmc*) (Fig. 4c, d). The coordinated upregulation of this range of target-killing components has not previously been described in the context of pathways that synergize with anti-PD-1 to potentiate CTL effector function. Perforin is a pore-forming cytolytic protein that facilitates the delivery of granzymes into target cells, thereby enabling apoptotic cell death.[85,86] Granzymes Gzmb, Gzmg, Gzmd, Gzme, Gzmf and Gzmk have reported cytotoxic functions.[87–91] Notably, Gzmk is associated with early-stage memory CD8⁺ T-cell differentiation.[92] Together, these findings position GSK-3 as a unique upstream amplifier of cytolytic programs for enhanced anti–PD-1–driven CTL immunity within the tumor microenvironment.

To further distinguish the transcriptional signatures associated with treatment responsiveness, we compared tumors from highly and poorly responsive mice. It was designated as a responder is there was a > 50% tumor volume reduction and a non-responder with a < 50% tumor volume reduction (otherwise a poor responder). TILs from both responders and non-responders expressed *Gzmg, Gzme, Gzmf, and Gzmd* (Fig. 4e). However, although *Gzmk, Gzmb, and Prf1* were expressed in non- or poorly responsive mice, the increase did not reach statistical significance. These results underscore the importance of a broad repertoire of cytolytic mediators for optimal tumor clearance. Among these, perforin, a pore-forming effector essential for CTL-mediated killing and is, in part, also regulated by PD-1 internalization,[25] while GZMB is well established as a key executor of CD8⁺ T-cell effector function in TILs.[93] Together, these data indicate that effective tumor regression requires the coordinated induction of the perforin–granzyme cytolytic program.

Gene set enrichment analysis (GSEA) also revealed a trend toward an enrichment of gene sets associated with T cell–mediated cytotoxicity and xenogeneic target cell killing (Supplementary Fig. 13). Consistent with this, analysis of an independently curated, unbiased cytolytic gene signature—including *Gzma, Gzmb, Prf1, Fasl, Ifng, Cd3e, Nkg7, Lgals1, Fgl2, Cxcl11, Nr4a3, Spp1, Icos, Klrg1, Cd8a, and Cd8b1*—demonstrated a significantly enhanced cytotoxicity score following combination therapy (Fig. 4f). Collectively, again, these findings indicate that GSK-3 inhibition cooperates with PD-1 blockade to reinforce transcriptional programs associated with cytolytic effector function.

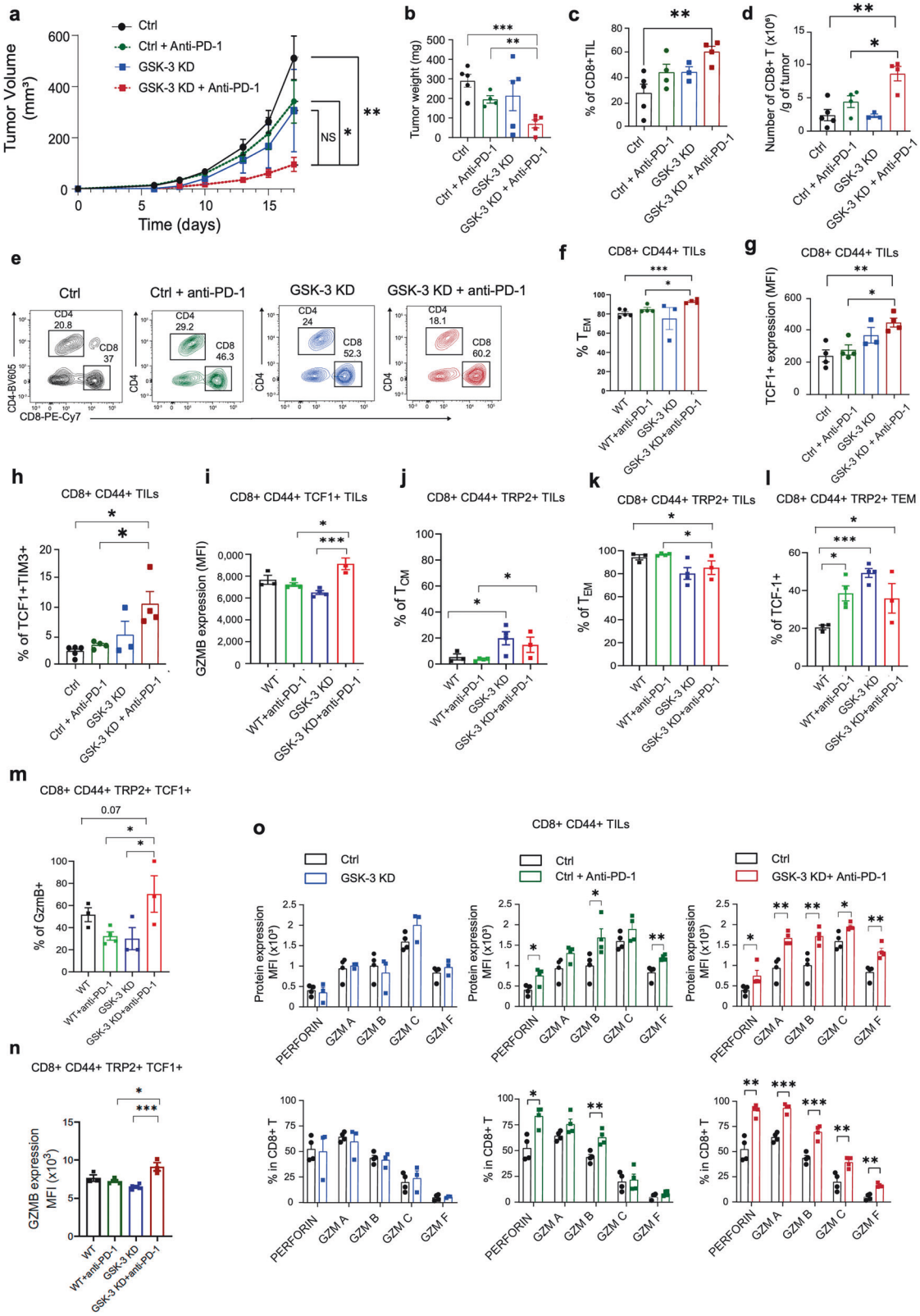
Notably, transcriptional profiling also revealed an elevated frequency of TCF-1⁺ cells within the CD8⁺ T_{CM} compartment (Fig. 4g) as well as an increase in *Tcf7* (TCF-1) expression following combination therapy (Fig. 4h). These findings suggest that GSK-3 inhibition, in concert with PD-1 blockade, both amplifies cytolytic effector programs and sustains the progenitor-like memory pool for a durable anti-tumor immunity.

GSEA also suggested an increase in glycolysis-associated genes with combination versus either monotherapy (Supplementary Fig. 14a, b). Consistently, an a priori pathway-defined gene set (GO/KEGG/Reactome) encompassing glycolysis and glucose import (*Slc2a1, Hk2, Pfkl, Aldoa, Pkm, Ldha, Hif1a, Slc16a3*) indicated a higher glycolysis score with combination therapy (Supplementary Fig. 14c, d). A pre-defined glucose import gene panel (*Slc2a1, Slc2a3, Akt1, Akt2, Pik3cd, Pik3ca, Mtor, Prkaa1, Tbc1d4, Insr*) showed an increased glucose import score in the combination group (Supplementary Fig. 14c, d).

GSK-3 KD licenses anti-PD-1 induction of CD8 multi-granzyme expression

These findings were also validated at the genetic level by analyzing the response of GSK-3 KD mice to anti–PD-1 therapy (Fig. 5a, b). Whereas anti–PD-1 monotherapy failed to significantly inhibit B16-F10 R1 tumor growth in WT mice, it produced a marked (> 75%) reduction in tumor burden in GSK-3 KD mice. This effect was evident by a measure of tumor volume (Fig. 5a) and tumor weight at day 17 post-implantation (Fig. 5b). These data confirmed that reduced GSK-3 expression synergizes with PD-1 blockade to suppress the growth of tumors otherwise resistant to immune-checkpoint monotherapy.

Further, anti–PD-1 synergy with the GSK-3 KD increased the presence of CD8⁺ TILs as a percentage (Fig. 5c) and in the number



of CD8⁺ TILs/gm of tumour (Fig. 5d). While untreated GSK-3 KD mice and anti-PD-1 treated WT mice showed an increase in CD8⁺ TIL frequency (Fig. 5c, rising from 24% to 42–44%), the combination of the two treatments yielded a synergistic effect to 60%. Likewise, the number of tumoral CD8 + T-cells increased from 2.4×10^6 cells/gm in the WT control to 9.2×10^6 cells/gm in GSK-3 KD mice. The increased presence of CD8 TILs was also clearly visible in a representative FACS plot (Fig. 5e).

Furthermore, combination therapy in mutant mice significantly enriched the T_{EM} TIL population (Fig. 5f). This expansion was

Fig. 5 Genetic GSK-3 knockdown licenses PD-1 blockade to generate super-armed, multi-granzyme-expressing CD8⁺ cytolytic T cells in the tumor microenvironment. **a**,**b** Tumor volume over time (**a**) and tumor weight at day 16 post-implantation (**b**) in WT and GSK-3 KD mice bearing B16-F10 R1 tumors, treated with or without anti-PD-1 antibody. Anti-PD-1 monotherapy was ineffective in WT mice but produced a > 75% reduction in tumor burden in GSK-3 KD mice. **c**,**d** Percentage of CD8⁺ cells among TILs (**c**) and absolute CD8⁺ TIL counts per gram of tumor (**d**) across treatment groups ($n = 3$–5). **e** Representative flow cytometry dot plots of CD4⁺ and CD8⁺ TIL fractions across treatment groups, illustrating the marked increase in CD8⁺ TIL proportion in anti-PD-1-treated GSK-3 KD mice. **f** Frequency of TEM cells within the CD8⁺CD44⁺ TIL compartment ($n = 4$). TEM TILs were significantly expanded in anti-PD-1-treated GSK-3 KD mice. **g** TCF-1 expression (MFI) within CD8⁺CD44⁺ TILs ($n = 3$–4). GSK-3 KD sustained elevated TCF-1 MFI, which was further increased by anti-PD-1 treatment. **h** Frequency of CD8⁺CD44⁺ TILs co-expressing TCF-1 and TIM-3 ($n = 3$), reflecting the emergence of a hybrid progenitor-exhausted state in GSK-3 KD mice. **i** GZMB expression (MFI) within CD8⁺CD44⁺TCF-1⁺ TILs ($n = 3$–4). Combined anti-PD-1 and GSK-3 KD significantly enhanced GZMB expression in TCF-1⁺ TILs. **j**,**k** Frequencies of TCM (**j**) and TEM (**k**) cells within the CD8⁺TRP2⁺ TIL population, identified using H-2K^b TRP-2 BV421 tetramers ($n = 3$–4). GSK-3 KD mice showed a shift toward central memory within the TRP-2-reactive TIL compartment. **l** Proportion of TCF-1⁺ cells within the CD8⁺TRP2⁺TEM TIL subset ($n = 3$–4). **m**,**n** GZMB co-expression within CD8⁺TRP2⁺TCF-1⁺ TILs, shown as frequency (**m**) and MFI (**n**) ($n = 3$–4). **o** Intracellular expression of perforin, GZMA, GZMB, GZMC, and GZMF in CD44⁺CD8⁺ TILs from WT and GSK-3 KD mice treated with or without anti-PD-1 ($n = 3$–5), shown as MFI (upper panels) and frequency of positive cells (lower panels). Anti-PD-1 treatment in GSK-3 KD mice markedly increased both the proportion and per-cell intensity of all cytolytic molecules assessed. Data are presented as mean ± s.e.m. Statistical comparisons were performed by unpaired two-tailed Student's t-test. *$P < 0.05$, **$P < 0.01$, ***$P < 0.001$, ****$P < 0.0001$; NS not significant. $n = 3$ independent experiments with 4–5 mice per group

accompanied by an increase in TCF-1 expression (MFI) in the CD8⁺ CD44⁺ TIL compartment of untreated GSK-3 KD mice- a trend further amplified by anti–PD-1 (Fig. 5g). Consistent with this, GSK-3 KD also increased the percentage of TCF-1⁺ TIM-3⁺ TILs within the CD8⁺ CD44⁺ TIL population (Fig. 5h). At the same time, CD8⁺CD44⁺TCF-1⁺ TILs showed an increase in GZMB expression from GSK-3 KD mice treated with anti–PD-1 (Fig. 5i). Collectively, these findings describe a hybrid phenotype in which GSK-3 deficiency bypasses the standard progression toward terminal exhaustion, instead preserving a TCF-1-high, effector-competent state in TIM+ exhausted cells, altering the differentiation landscape of the TILs.

For the identification of tumor-reactive TILs from B16-F10 tumors, we used H-2K^b TRP-2 BV421 tetramers (mouse MHC class I; TRP-2_180–188 (SVYDFFVWL)) to identify TRP-2–specific TILs. TRP-2 (tyrosinase-related protein 2) is a melanocyte differentiation antigen expressed by B16 melanoma cells. TILs isolated from B16-F10 tumors at day 18 were assessed for differentiation status and expression of TCF-1 and GZMB. GSK-3 KD mice showed an increase in the percentage of CD8⁺CD44⁺TRP2⁺ T_{CM} cells in untreated and anti–PD-1-treated mice (Fig. 5j). While CD8⁺CD44⁺TRP2⁺ TILs predominantly displayed a T_{EM} phenotype in both genotypes, GSK-3 KD mice showed a reduction in T_{EM} cells that was roughly commensurate with the increase in T_{CM} cells (Fig. 5k). Importantly, the proportion of the CD8⁺TRP2⁺ T_{EM} subset expressing TCF-1⁺ was elevated in GSK-3 KD mice (Fig. 5l). Anti–PD-1 treatment increased the frequency of TCF-1⁺ CD8⁺CD44⁺TRP2⁺ TILs in WT mice from 21 to 39%, approximating the levels observed in untreated and anti-PD-1 treated GSK-3 KD mice. Collectively, these findings indicate that GSK-3 KD enriches the TRP2⁺ CD8⁺ TIL compartment for central memory differentiation and promotes a TCF-1⁺ memory-like transcriptional program within the T_{EM} subset.

Moreover, within the TCF-1⁺ compartment, co-expression of GZMB was significantly enriched in CD8⁺CD44⁺TRP2⁺TCF1+TILs from anti-PD-1 treated GSK-3 KD mice relative to the untreated GSK-3 mice and anti-PD-1 treated WT mice (Fig. 5m). Further, this was accompanied by an increase in the GZMB MFI in anti-PD-1 treated GSK-3 KD mice (Fig. 5n). GSK-3 down-regulation favors the accumulation of TCF-1⁺, memory-biased CD8⁺ TILs, while PD-1 blockade enhances their cytolytic competence, giving rise to a distinct TCF-1⁺GZMB⁺ effector–memory hybrid state within the tumor.

Further underscoring this, flow cytometric analysis of intracellular granzymes revealed that anti–PD-1 treatment in GSK-3 KD mice markedly upregulated the expression of perforin and multiple granzymes—GZMA, GZMB, GZMC, and GZMF—as determined using validated anti-granzyme antibodies (Fig. 5o). Other granzymes could not be reliably assessed due to the lack of antibodies suitable for flow cytometry detection. While anti–PD-1 monotherapy modestly increased the frequency of GZMB-expressing CD8⁺ T cells in WT mice, the combination of anti–PD-1 and GSK-3 KD significantly enhanced both the mean fluorescence intensity (MFI) of perforin and granzyme expression (upper panels) and the percentage of CD8⁺ T cells expressing perforin and multiple granzymes GZMA, GZMB, GZMC and GZMF (lower panels). Consistent with our findings using pharmacological GSK-3 inhibition, these results demonstrate that genetic down-regulation of GSK-3 synergizes with PD-1 blockade to increase the cytolytic capacity of CD8⁺ TILs with the coordinated upregulation of perforin and a broad repertoire of multiple granzymes.

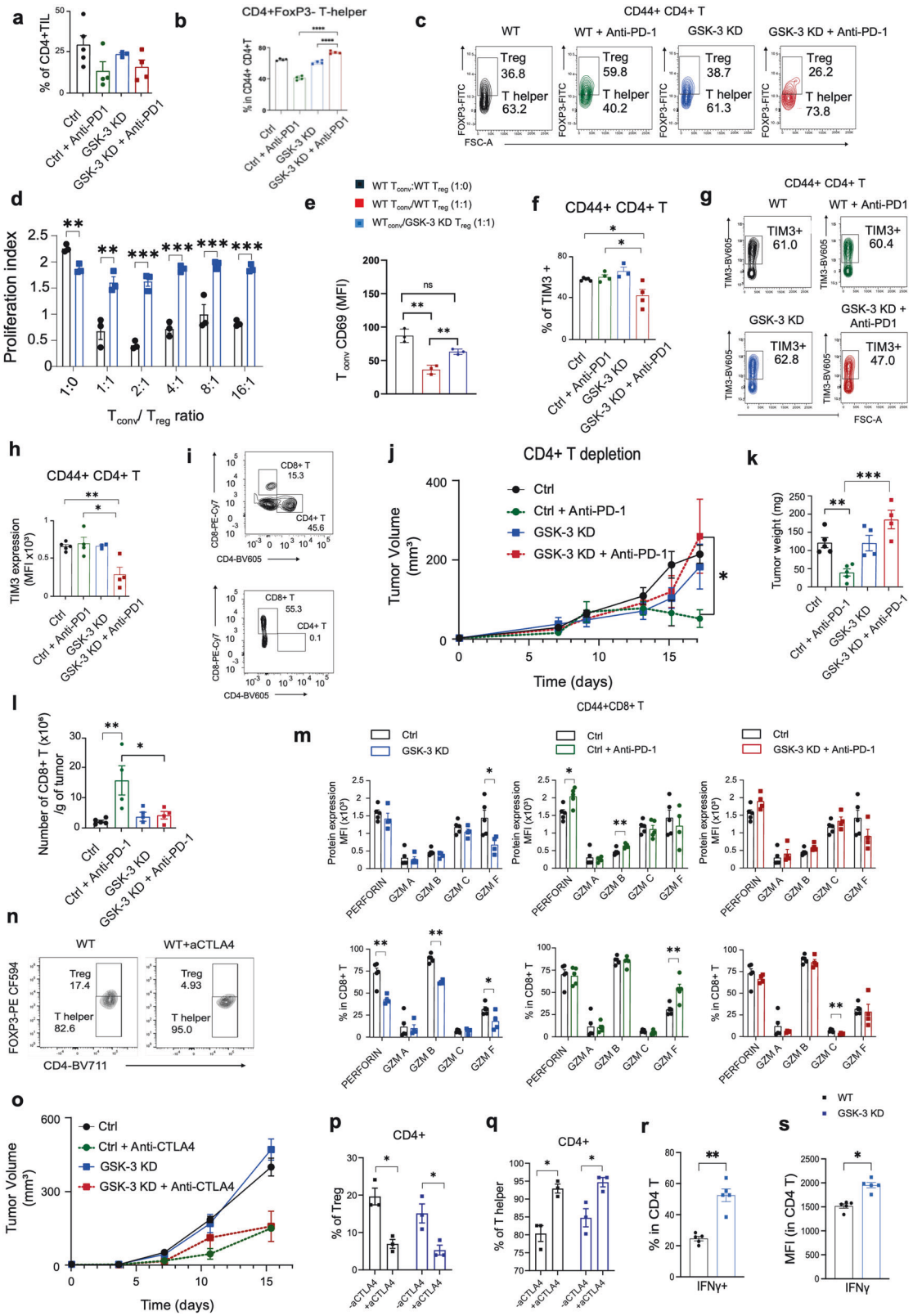
GSK-3 regulates Treg/Th balance and CD4 + T-helper dependency

A key next question was whether the induction of granzymes by combination therapy was driven by a role for GSK-3 in regulating CD4⁺ T-cell help for CD8⁺ T cells (Fig. 6). CD4⁺ T-cell help facilitates CD8⁺ T-cell differentiation and effector function.[4–6] We therefore first examined the impact of GSK-3 KD on CD4⁺ T-cell populations in the TME.

Firstly, we examined the status of CD4 TILs in WT versus GSK-3 KD mice. The down regulation of GSK-3 did not significantly alter the overall frequency of CD4⁺ TILs (Fig. 6a). However, TILs in the GSK-3 KD mice showed an increase in the presence of CD4⁺FOXP3⁻ helper T cells (Fig. 6b). This was especially evident in a comparison of the effects of anti-PD-1 in GSK-3 KD vs WT mice (Fig. 6b). A representative FACS plot shows that anti–PD-1 reduced helper T cells to 40.2% of total CD4⁺ TILs in WT mice, while dramatically increasing to 73.8% in GSK-3 KD mice (Fig. 6c). Conversely, the frequency of CD4⁺FOXP3⁺ Tregs increased from 36.8 to 59.8% in WT mice treated with anti–PD-1, as in previous reports.[94–97] However, their presence was markedly decreased to 26.2% in GSK-3 KD mice commensurate with the increase in CD4+ helpers. These results indicated that GSK-3 down regulation shifts the intratumoral CD4⁺ T-cell balance away from suppressive Tregs and toward helper subsets in the context of anti-PD-1 immunotherapy, thereby potentially enhancing the available CD4-dependent support for CD8⁺ effector T-cell responses.

To determine whether GSK-3 is required for Treg suppressor function, we compared the inhibitory capacity of WT versus GSK-3 KD Tregs in vitro (Fig. 6d, e). Purified CD4⁺CD25⁺ Tregs were co-cultured with increasing numbers of Tag-it–labelled wild-type conventional CD4⁺CD25⁻ responder T cells (Tconv) in the presence of soluble anti-CD3 and mitomycin C–inactivated splenocytes as feeder cells (see Materials and Methods). After 72 h, Tresp proliferation was quantified to assess Treg-mediated suppression.

Wild-type Tregs robustly suppressed responder T-cell proliferation, reducing the proliferation index across all Tconv:Treg ratios tested (black columns, Fig. 6d). Proliferation was reduced by 80%



at a 2:1 ratio and by 50% at an 8:1 ratio. In striking contrast, GSK-3 KD Tregs were profoundly impaired in exercising suppression, achieving only 10% inhibition at a 1:1 ratio. Consistent with this loss of function, WT Tregs reduced expression of the activation marker CD69 on Tconv cells by over 50%, whereas GSK-3 KD Tregs had no significant effect (Fig. 6e). Together, these findings establish GSK-3 as an essential regulator of Treg suppressive function, highlighting its critical role in sustaining immune regulation and peripheral tolerance

Anti–PD-1 treatment in GSK-3 KD mice also reduced both the frequency and surface expression intensity of the exhaustion marker TIM-3 on CD4⁺CD44⁺ TILs (Fig. 6f). A representative flow-

Fig. 6 GSK-3 coordinates CD4⁺ T-cell helper–Treg balance and is required for CD4⁺ help-dependent CD8⁺ cytolytic function during PD-1 blockade. **a** Total CD4⁺ TIL frequency in WT and GSK-3 KD mice with or without anti-PD-1 treatment. No significant difference in overall CD4⁺ TIL abundance was observed between genotypes. **b**,**c** Frequencies of CD4⁺FOXP3⁻ helper T cells (**b**) and CD4⁺FOXP3⁺ Tregs (**c**) within the CD4⁺CD44⁺ TIL population ($n = 3$). Representative flow cytometry plots (**c**) demonstrate that anti-PD-1 treatment increased helper T cells to 73.8% of CD4⁺ TILs in GSK-3 KD mice (versus 40.2% in WT), while concomitantly reducing $T_{AE}{}^{H}$ to 26.2% (versus 59.8% in WT). **d**,**e** GSK-3 expression is needed for Treg mediated suppression of the proliferation of conventional T-cells. In vitro Treg (T_{reg}) suppression assay profiles using different Tconv:Treg ratios where the proliferation of prelabelled conventional T-cells (T_{conv}) was quantified by dye dilution (**d**; $n = 3$). CD69 expression on conventional T-cells was measured as a secondary readout (**e**). **f–h** TIM-3 expression is reduced on GSK-3 KD CD44⁺CD4⁺ TILs: frequency of TIM-3⁺ cells (**f**; $n = 3$–4), representative flow cytometry dot plots (**g**), and TIM-3 MFI (**h**; $n = 3$–5). Anti-PD-1 treatment in GSK-3 KD mice reduced both the frequency (from 60.4 to 47.0%) and the intensity of TIM-3 expression on CD4⁺ TILs. **i** Representative flow cytometry dot plot confirming efficient in vivo CD4⁺ T-cell depletion following anti-CD4 antibody administration (300 µg i.p. at days −1, 7, and 14). **j**,**k** Tumor volume (**j**) and tumor weight (**k**) following CD4⁺ T-cell depletion in WT and GSK-3 KD mice treated with anti-PD-1. In WT mice, CD4⁺ depletion enabled anti-PD-1-mediated tumor regression (consistent with removal of T_{reg} mediated suppression). Conversely, CD4⁺ depletion completely abrogated the anti-tumor efficacy of anti-PD-1 in GSK-3 KD mice, resulting in rapid tumor outgrowth. **l** CD8⁺ TIL counts per gram of tumor following CD4⁺ depletion. CD4⁺ depletion prevented anti-PD-1-driven CD8⁺ TIL expansion in GSK-3 KD mice. **m** Expression of perforin, GZMA, GZMB, GZMC, and GZMF in CD44⁺CD8⁺ TILs following CD4⁺ T-cell depletion in GSK-3 KD mice treated with anti-PD-1, shown as MFI (upper panels) and frequency of positive cells (lower panels). CD4⁺ depletion markedly reduced granzyme and perforin expression, demonstrates the indispensability of CD4⁺ helper signals for the super-armed CTL phenotype. **n** Representative flow cytometry dot plot confirming in vivo T_{reg} depletion following anti-CTLA-4 antibody treatment (200 µg i.p. at days 4, 7, and 10). **o** Tumor volume in WT and GSK-3 KD mice following anti-CTLA-4-mediated T_{reg} depletion ($n = 3$–4). Anti-CTLA-4 promoted tumor regression in WT mice but conferred no additional benefit in GSK-3 KD mice, which already achieved effective tumor control. **p**,**q** Frequency of T_{regs} (**p**) and CD4⁺FOXP3⁻ helper T cells (**q**) among CD4⁺ TILs following anti-CTLA-4 treatment ($n = 3$). Anti-CTLA-4 selectively depleted Tregs while expanding the helper T-cell fraction. **r**,**s** IFN-γ production by CD4⁺ TILs in WT versus GSK-3 KD mice, expressed as frequency of IFN-γ⁺ cells (**r**) and MFI (**s**). GSK-3 KD CD4⁺ TILs produced significantly more IFN-γ, providing a potential mechanistic basis for enhanced CD4⁺-mediated support of CD8⁺ cytolytic responses. Data are presented as mean ± s.e.m. Statistical comparisons were performed by unpaired two-tailed Student's t-test. $^{*}P < 0.05$, $^{**}P < 0.01$, $^{***}P < 0.001$, $^{****}P < 0.0001$; NS not significant. $n = 4$–5 mice per group

cytometry plot demonstrates a decrease in TIM-3⁺ cells from 60.4% in WT mice to 47.0% in GSK-3 KD mice (Fig. 6g). The MFI of TIM-3 expression was likewise diminished in GSK-3 KD mice treated with anti–PD-1 (Fig. 6h). The same treatment had no effect on TIM-3 expression in WT mice. Together, these data indicate that anti–PD-1 synergizes with reduced GSK-3 activity to limit TIM-3 upregulation—an inhibitory receptor commonly associated with T-cell dysfunction in chronic settings—thereby potentially promoting improved CD4⁺ helper function and downstream CD8⁺ effector activity.

Given the pronounced alterations in the CD4⁺ T-cell compartment, we next assessed the functional contribution of CD4⁺ T cells by depleting them at multiple time points before and during anti–PD-1 therapy (Fig. 6i, j). Anti-CD4 depletion efficiently reduced the presence of CD4⁺ T cells from 45.6% in untreated controls to 0.1% in CD4-depleted mice (Fig. 6i and Supplementary Fig. 15a). Strikingly, CD4 depletion enabled anti–PD-1 therapy to induce robust rejection of B16-F10 R1 tumors in Ctrl (WT) mice, as reflected by significant reductions in both tumor volume and tumor weight (Fig. 6j, k, respectively). This contrasted with the lack of an effect of anti-PD-1 on tumor growth in normal non-depleted WT mice (Fig. 5a). These findings suggested that the anti-CD4 depletion alleviated immunosuppression, mostly likely via the depletion of CD4+ Tregs, effectively restoringPD-1–mediated tumor control.

Conversely, in GSK-3 KD mice, which displayed an increased frequency of CD4⁺ helper T cells, CD4 depletion generated a different result by completely abrogating the therapeutic efficacy of anti–PD-1. This loss of response was evident from the resumption of rapid tumor growth and the marked increase in tumor burden (Fig. 6j, k). In contrast to WT mice—where anti–PD-1 treatment promoted robust CD8⁺ TIL accumulation—the same therapy failed to expand the CD8⁺ TIL population in GSK-3 KD mice following CD4 depletion (Fig. 6l).

Importantly, the absence of CD4⁺ T-cell help, in GSK-3 KD mice, also abrogatedthe anti–PD-1–induced upregulation of cytotoxic effector molecules within the CD8⁺ TIL compartment. Expression of perforin, GZMA, GZMB, GZMC, and GZMF was markedly reduced, as reflected by decreases in both the MFI (upper panel) and the percentage of granzyme-expressing cells (lower panel) (Fig. 6m). These results indicate that GSK-3 deficiency enhances CD8⁺ effector responses through CD4⁺ T-cell help, and that this helper function is indispensable for sustaining PD-1 blockade–mediated tumor control.

To further confirm the contribution of Treg-mediated suppression to the anti-tumor response, we examined the effects of Treg depletion using anti–CTLA-4 treatment (Fig. 6n, o). Administration of anti–CTLA-4, which effectively depleted CD4⁺FOXP3⁺ Tregs (Fig. 6n; Supplementary Fig. 15b), resulted in a pronounced reduction in tumor size in both WT and GSK-3 KD mice Fig. 6o). However, while anti–CTLA-4 facilitated tumor regression in WT mice, it produced no additional benefit in GSK-3 KD mice, where tumors were efficiently rejected. In other words, GSK-3 KD mice rejected B16-F10 R1 tumors irrespective of Treg depletion, whereas WT mice required Treg removal to achieve comparable tumor control. This finding contrasts with the earlier observation that anti-CD4 treatment impaired tumor regression in GSK-3 KD mice (Fig. 6j). As a control, anti–CTLA-4 treatment significantly reduced the number of CD4⁺FOXP3⁺ Treg TILs (Fig. 6p), while increasing the presence of CD4⁺FOXP3⁻ conventional T cells (Fig. 6q), confirming the selectivity of Treg depletion.

Collectively, these results indicate that while both anti-CD4 and anti–CTLA-4 target CD4⁺ subsets, their functional outcomes differ fundamentally. Loss of CD4⁺ helper cells in GSK-3 KD mice abolished anti–PD-1–mediated tumor regression, whereas Treg depletion had no additional effect, suggesting that reduced GSK-3 expression heightens CD8⁺ T-cell dependence on CD4⁺ helper signals. As expected, depletion of CD8⁺ T cells impaired tumor control in both WT and GSK-3 KD mice (Supplementary Fig. 16), confirming the central role of cytotoxic T cells in mediating tumor rejection.

Finally, to elucidate potential mechanisms underlying CD4⁺ helper activity, we analyzed cytokine production in GSK-3 KD CD4⁺ T cells. These cells exhibited a striking increase in IFN-γ production, as demonstrated by elevations in the frequency of IFN-γ–expressing CD4⁺ T cells (Fig. 6r) while also increasing the level of IFN-γ expression as expressed as an MFI (Fig. 6s). Enhanced IFN-γ secretion by CD4⁺ T cells promotes CD8⁺ T-cell activation, survival, and cytolytic function, providing a potential mechanism by which CD4⁺ help sustains effective antitumor CTL responses.

Together, these findings demonstrate that CD4⁺ T-cell subsets exert context-dependent effects on PD-1 blockade: in WT mice, CD4⁺ Tregs constrain anti-tumor immunity, whereas in the GSK-3 KD setting, CD4⁺ helper T cells play the dominant role for maintaining CD8⁺ T-cell cytotoxicity and achieving durable tumor control.

DISCUSSION

Despite its role in T-cell signaling, the contribution of GSK-3 to immune checkpoint blockade (ICB) remains largely unexplored. Here we have identified GSK-3 as a key regulator of TCF-1$^+$ progenitor and memory CD8$^+$ T-cell differentiation, where reduced GSK-3 expression enhances antiviral and antitumor immunity. GSK-3 maintains the homeostatic balance of peripheral T cells; during chronic LCMV Cl13 infection, its KD promotes the expansion of GP33-specific MPECs and memory T cells. Metabolic profiling revealed elevated OXPHOS, glycolytic capacity, and GLUT1 expression in GSK-3–KD TCF-1$^+$ stem-like CD8$^+$ T cells. It also promoted an increase in mitochondrial mass in all CD8+ subsets. Importantly, GSK-3 inhibition or down-regulation enabled anti–PD-1 therapy to overcome tumor resistance by reducing CD4$^+$ Treg involvement and enhancing TEM CD8$^+$ populations. This synergy generated "super-armed" cytolytic T cells expressing a remarkable seven granzymes (GZMB–G). Reduced GSK-3 was essential for CD4$^+$ helper collaboration with CD8$^+$ T cells to achieve this induction. Thus, GSK-3 is a central checkpoint integrating metabolism, CD4–CD8 cooperation, and cytolytic reprogramming.

We first demonstrated in CD4 and CD8 T-cells from naïve, unchallenged mice that the GSK-3 knockdown mice exhibit a significant, T-cell-intrinsic shift from a quiescent phenotype (CD44^{lo}) to an activated/memory-phenotype (CD44^{hi}, CD62L$^+$) status. Specifically, CD8 + T-cells showed a shift in differentiation to both central memory (CM) and effector memory (EM) subsets. This is a novel finding that moves beyond GSK-3's established role as a negative regulator of T-cell activation and demonstrates that GSK-3 is an essential master molecular switch that actively represses the differentiation program to maintain the T-cell pool's fidelity to a quiescent, naïve homeostatic state. The extent to which this altered pre-existing state in GSK3 KD mice influenced the mice's enhanced resistance to viral infection and cancer remains an interesting question.

During chronic viral infection, GSK-3 KD favored CD8$^+$ TCF-1$^+$ progenitors, MPECs, and memory subsets over naïve and terminal effectors. MPECs exhibited elevated GLUT1 and glucose uptake, indicating enhanced metabolic fitness. Their expansion, alongside reduced SLECs, shows that GSK-3 deficiency promotes memory-precursor differentiation. As MPECs represent the principal source of long-lived T_{CM} and T_{EM} T cells,[68,98] their expansion, together with the concomitant reduction in SLECs, indicates that GSK-3 deficiency promotes memory-precursor differentiation during the resolution of chronic infection. The CD8$^+$ TCF-1$^+$ subset displayed the highest Ki-67 expression, underscoring enhanced self-renewal. The frequency of IFN-γ$^+$ GP33$^+$ CD8+-cells at day 30 of infection increased from 24 to 82% in GSK-3 KD mice indicating that the reduction in GSK-3 reversed T-cell exhaustion. These findings position GSK-3 as a regulator exhaustion and the presence of stem-like TCF-1$^+$ T cells—a population essential for antiviral immunity[99] and clinically relevant in conditions like COVID-19[100]

Notably, the GSK-3 KD mice also generated a unique hybrid phenotype of CD8$^+$+ CD44$^+$ TCF-1$^+$ T-TILs expressing *Gzmb*, a deviation from the expected inverse relationship where TCF-1$^+$ progenitor-exhausted (TPEX) cells normally have low to immediate GZMB, while TCF-1$^-$ subsets carry the cytolytic program. These hybrid cells likely provide a renewable source of TILs that maintain proliferative fitness while executing anti-tumor function, explaining the synergy between GSK-3 inhibition and PD-1 blockade.

Further, Seahorse and SCENITH analyses showed that GSK-3 KD enhanced both glycolytic and OXPHOS programs, particularly in TCF-1$^+$ TPEX cells. This dual enhancement supports metabolic agility, allowing cells to pivot energy sources based on availability. In chronic LCMV infection, GSK-3 KD promoted oxidative metabolism and mitochondrial fitness within the TPEX compartment. Consistent with established metabolic remodeling during T-cell activation, Seahorse assays further showed elevated glycolytic and OXPHOS activity following anti-CD3 stimulation, with a disproportionately strong increase in glycolysis—reflecting the transient shift toward aerobic glycolysis that accompanies effector differentiation.[101,102] Together, these data indicate that GSK-3 inhibition promotes metabolic flexibility, enabling CD8$^+$ T cells to dynamically promote glycolysis during activation while preserving an OXPHOS-dependent, stem-like metabolic state.[103]

We observed a selective increase in GLUT1 on GSK-3 KD TPEX cells, but not on terminally exhausted cells. While the role of GLUT1 expression in exhaustion is debated,[104] our data indicate GSK-3 is a primary regulator of GLUT1, favoring the TPEX subset. In other contexts, such as chronic human viral infections, GLUT1 expression has been reported as higher on certain chronically activated cells (e.g., HBV-specific CD8 + T cells).[105] This suggests that GLUT1 levels are governed by context- and tissue-specific regulation rather than a universal rule. Regardless, our data indicate that GSK-3 acts as a prime regulator of GLUT1 expression, specifically favoring the TPEX subset.

Furthermore, GSK-3 acts as an upstream regulator of mitochondrial abundance. Although KD increased mitochondrial content across all subsets, only TPEX cells exhibited enhanced plasticity, suggesting that mitochondrial mass alone cannot overcome the metabolic rigidity of terminal exhaustion. Nevertheless, the enhanced presence of mitochondria in all CD8 exhaustion subsets would be expected to generate ATP needed for their sustained function. GSK-3 also regulates mitochondrial mass during muscle myogenesis.[106]

Since progenitor TCF-1$^+$ T cells are required for successful anti–PD-1 therapy, we anticipated that GSK-3 inhibition—using either small-molecule inhibitors (SMIs) or genetic downregulation—could cooperate with anti–PD-1 to eliminate tumors normally resistant to checkpoint blockade. Indeed, this prediction proved correct: tumor growth reduction was observed only with the combination therapy in both the B16-F10-R1 and MC38 tumor models. In the melanoma model, tumor growth was unaffected by either monotherapy but was reduced by more than 70% by day 16 under combination treatment. Tumor regression was accompanied by a significant shift in the TME, as CyTOF analysis revealed a marked reduction in highly suppressive FOXP3^{hi} CD25$^+$ regulatory T cells, alongside an increase in T_{EM} TILs. The abundance of T_{EM} cells correlated with reduced tumor mass. In contrast, CD8$^+$ T_{EFF} cells exhibited only a trend toward expansion and were not associated with tumor rejection, possibly due to their shorter lifespan. Collectively, these findings highlight GSK-3 as a central regulator of the balance between suppressive Tregs and CD8$^+$ T_{EM} cells in the tumor microenvironment during anti–PD-1 therapy.

Transcriptomic analysis showed that GSK-3 downregulation modulated the T-cell response to anti–PD-1 therapy by enabling checkpoint blockade to regulate many more genes than are normally induced by anti–PD-1 alone. The effect was particularly pronounced in immune-associated genes. Among the 37 genes upregulated by combination therapy, there was a striking increase in the expression of seven granzymes (GZMB, GZMK, GZMG, GZME, GZMF, GZMD, GZMC), all with the potential to mediate tumor killing. Perforin, a pore-forming protein essential for CTL cytotoxicity, was also induced.[107] To our knowledge, this is the first demonstration of a single protein capable of "super-arming" cytolytic T cells, thereby enhancing their capacity for tumor destruction. Multiple granzymes—including GZMB and granzymes D, E, and F—have previously been implicated in T-cell–mediated cytotoxicity.[87] In the context of GSK-3 inhibition, granzyme K (GZMK) is notable for its association with early-stage memory CD8$^+$ T-cell differentiation,[92] the induction of proinflammatory responses,[88] and activation of the complement-mediated killing cascade.[89] Moreover, GZMC and GZMK utilize caspase-independent cytotoxic pathways,[32] whereas GZMF triggers Bid-independent cytochrome c–mediated apoptosis[90] and IL-15–driven induction of GZMC contributes to ILC1-mediated tumor killing.[91]

How these components interface with each other is not yet known, but perforin and certain granzymes can act synergistically or with functional redundancy to ensure a robust and reliable cytotoxic response. Their diversity provides an advantage, as each granzyme cleaves distinct cellular targets, collectively broadening the spectrum of tumor cell killing. For example, the granzyme profile induced here excluded GZMH, indicating a GSK-3–dependent regulatory program that selectively upregulates GZMB and GZMC–G. This pattern aligns with a possible shift toward caspase-dependent apoptotic killing, rather than caspase-independent inflammatory death. To our knowledge, the coordinated induction of such a broad array of granzymes within immune effector cells is unprecedented.

Analysis by both CyTOF and conventional flow cytometry revealed a trend toward a decreased relative presence of $CD4^+$ tumor-infiltrating lymphocytes (TILs). This reduction was even more pronounced within the regulatory T-cell compartment, particularly among $CD4^+FOXP3^{hi}CD25^+$ cells, in response to combined GSK-3 inhibition and anti–PD-1 therapy. Further flow cytometric analysis using fluorescent antibody staining confirmed that anti–PD-1 treatment reduced the frequencies of $PD\text{-}1^+FOXP3^+$ and $TIM\text{-}3^+FOXP3^+$ Tregs, with a modest additional decrease observed in GSK-3 KD mice relative to WT controls.

Functionally, GSK-3 reduction impaired the suppressive capacity of Tregs, as demonstrated by classical suppression assays in which $CD4^+CD25^+$ T cells were titrated into co-cultures with anti-CD3 and proliferation dye–labeled conventional $CD4^+CD25^-$ T cells. Notably, during the resubmission of this manuscript, an independent study also showed that GSK-3 is required for both Treg development and suppressive function.[108] Together, these findings identify an additional mechanism through which GSK-3 modulates $CD8^+$ T-cell responses during infection and tumor immunity.

However, the impact of $CTLA\text{-}4^+$ Treg depletion on tumor growth was not evident in GSK-3 KD mice, as these animals already exhibited effective tumor control. Although GSK-3 regulation of Treg function may contribute to tumor growth control under certain conditions, its role in this setting was not decisive. In contrast, WT mice required $CTLA\text{-}4^+$ Treg depletion to achieve tumor rejection. In WT animals, both anti-CD4 and anti–CTLA-4 treatments enabled tumor regression, highlighting the multifaceted role of GSK-3 in balancing effector and regulatory T-cell responses within the tumor microenvironment.

Mechanistically, our study directly implicated GSK-3 in the regulation of CD4 + T helper function for enhanced tumor rejection in response to anti-PD-1 blockade. CD8 + T-cell function depends on CD4 + T-cell help.[2,6] Our data identify GSK-3 as a pivotal regulator of $CD4^+$ helper function that sustains effective $CD8^+$ T-cell responses during PD-1 blockade. Reduced GSK-3 expression creates a dependency on $CD4^+$-derived help, possibly via essential IFN-γ which is well documented to support for $CD8^+$ T-cell activation, persistence, and cytotoxicity. In contrast, when GSK-3 expression is intact, Treg-mediated suppression predominates, and tumor control improves only after Treg removal. Thus, GSK-3 determines the balance between suppressive and helper $CD4^+$ subsets, shaping the quality of the $CD8^+$ effector response and the overall outcome of checkpoint therapy. Overall, our findings in this paper related to GSK-3 regulation of CD4-CD8 collaboration in the generation of CD8 CTLs could provide a mechanism to explain the past findings showing that GSK-3 can promote CAR function and tumor rejection.[42,56–58,61–63]

While prior work using small-molecule inhibitors (SMIs) suggested a role for GSK-3 in memory,[109] our genetic model establishes a direct link. Differences with GZMB-Cre knockout models—which reported increased exhaustion[110]—likely stem from our use of the distal Lck promoter, which targets T-cell lineages differently than models affecting broader immune subsets like NK cells or eosinophils.[111] This phenomenon is particularly relevant for Tregs, where granzyme B can contribute to their suppressive function.[112] Our KD mouse also shows a complete loss of GSK-3β, while retaining some 50% levels of GSK-3α. The reduced expression of one isoform relative to a nother may elicit different downstream effects.

It is likely that a pathway triggered by anti–PD-1 blockade cooperates with signaling networks unleashed by GSK-3 reduction to drive transcriptional programs that upregulate multiple granzymes. GSEA analysis confirmed that combining GSK-3 inhibition with anti–PD-1 promoted the expression of genes associated with T-cell–mediated cytotoxicity, including those encoding granzymes and perforin. The pathway is not expected to be the only pathway. For example, as mentioned, GSK-3 is a known negative regulator of NFAT, while T-bet and EOMES which also regulate the perforin and several granzyme promoters. Another pathway involves β-catenin which is upregulated in our GSK-3 KD T-cells. When GSK-3 is downregulated, β-catenin is less phosphorylated and degraded, leading to its translocation to the nucleus as a co-activator for TCF/LEF transcription factors. TCF-1 (encoded by *tcf-7*) can drive its own expression in T cells, while concurrently repressing PRDM1 (Blimp-1), TBX21 (T-bet), IFN-γ, GZMB, and PDCD1 (PD-1). As we showed previously, GSK-3 inhibition can substitute for CD28 co-stimulatory signals[61,113] and downregulate PD-1 and LAG-3.[42,57] Further work is needed to pinpoint the key transcription factors unleashed by the reduction of GSK-3 activity and expression.

Our murine findings are consistent with emerging human data indicating that the potential benefit of targeting GSK-3 activity. The Goronzy laboratory reported that GSK3β inhibition restored the activation and cytokine production of aged T cells,[109] whereas the Sampath laboratory reported that GSK-3 inhibition improved CAR-T-cell function while reducing PD-1 levels[111,114] in keeping with our previous paper showing that GSK-3 modulates PD-1 and LAG-3 for better tumor elimination.[42,58,115] In conclusion, our data shows that the targeting GSK-3 expands the pool of PD-1-responsive progenitor T cells and enhances metabolic fitness, providing a mechanistic framework for combining GSK-3 inhibitors with checkpoint therapy in human cancer.

MATERIALS AND METHODS

Animals and animal care

TGSK-3αflox/flox βflox/flox mice were produced by crossing GSK-3 alpha(flox/flox) and GSK-3 beta (flox/flox) mice to generate double-GSK-3 αflox/flox βflox/flox mice. GSK-3 αflox/flox βflox/flox mice were then bred with distal dLCK-Cre mice (B6.Cg-Tg(Lck-icre)3779Nik/J, Jackson Laboratory, Maine) to delete the GSK-3α and GSK-3β isoforms. All experimental animals were maintained on a C57BL/6J genetic background and were age and sex-matched for each cohort. Genotypes were confirmed by PCR analysis of genomic DNA extracted from the distal end of the tail. DNA was amplified using specific primers for the dLck-cre transgene (foward: ATGGTGCCCAAGAAGAAGAG, reverse: CAGGTGCTGTTGGATGGTCT), and the expression of GSK3α (forward: CCCCCACCAAGTGATTTCACTGCTA, reverse: CTTGAACCTTTT GTCCTGAAGAACC) and GSK3β (forward: GGGGCAACCTTAATTT-CATT, reverse: GTGTCTGTATAACTGACTTCCTGTGGC) flox genes. Thermal cycling conditions consisted of an initial denaturation at 95°C for 15 minutes (enzyme activation and first denaturation), followed by 30 cycles of 95°C (30s, denaturation), 55°C (45s, annealing), and 72°C (60s, extension). Intercrossing of the parental lines resulted in a partial reduction of GSK-3 expression in T-cells (referred to as GSK-3 knock down mice). Immunoblotting showed a greater loss of the alpha than that beta forms. All animals were housed in a pathogen-free facility under a 12-hour light/dark cycle with ad libitum access to sterile water and standard irradiated chow. Health monitoring was performed quarterly, confirming the absence of common murine pathogens. Mice were maintained in cages equipped with filtered tops. While both male and female

mice were utilized. Sex was not incorporated as a biological variable in the study design or statistical analysis. All animal procedures were performed in accordance with the guidelines.

Cell lines

B16 F10 and MC38 tumor cells were maintained in DMEM supplemented with 10% FCS, 1% L-glut and 1% Pen/Strep. Tumor cells (2×10^5) cultured for less than two weeks were implanted subcutaneously in the flank of recipient mice using 29G1/2 syringes. Tumor size was monitored using a manual caliper and tumors were excised before exceeding the volume permitted by CR-HMR ethic committee.

Isolation and stimulation of **T-**cells

Spleens were harvested from mice, and single-cell suspensions were prepared by mechanical dissociation through a 70 µm cell strainer. Red blood cells were lysed using ACK Lysis Buffer, and $CD8^+$ T cells were subsequently purified by magnetic-activated cell sorting (MACS) according to the manufacturer's protocol. Purified $CD8^+$ T cells were labeled with CellTrace™ Violet (Tagit Violet™, Thermo Fisher Scientific) for proliferation tracking and cultured at a density of 1–2 × 10^6 cells/ml in RPMI 1640 medium supplemented with 10% heat-inactivated fetal bovine serum (FBS) and penicillin–streptomycin. Cells were stimulated in vitro with graded concentrations of soluble anti-CD3 antibody (clone 2C11, 0.005–2 µg/ml) for 72 h.

LCMV viral infections

Mice were acclimated in a biosafety level 2 (BSL2) facility the day prior to infection. On the day of inoculation, frozen lymphocytic choriomeningitis virus (LCMV) stocks were thawed rapidly and placed on ice. Virus was diluted to the 2 × 106 plaque-forming units (PFU)/200 µL (Clone 13) or 2 × 105 PFU/200 µL (Armstrong) in sterile phosphate buffered saline lacking Ca2+ and Mg2 + . Clone 13 was injected intravenously (i.v.) whereas the Armstrong strain was injected via the intraperitoneal (i.p.) route.

At the experimental endpoint of each experiment, spleens were extracted to study the composition and phenotype of viral-specific CD8 T-cells by GP33 tetramer staining. Spleens were mechanically dissociated, subjected to red blood cell lysis, and resuspended in 8 mL of 2% HBSS. Cells were distributed into a 96-well plate at 200 µL per well (≥4×10^6 cells each well). Plates were spun at 500 × g for 5 min at 4 °C. The GP33 reactive T-cells were detected using H-$2D^b$–KAVYNFATM–BV421 tetramers (National Institutes of Health (NIH) Tetramer Core Facility). These tetramers were diluted 0.8 µL per 50 µL 2% HBSS and added to the pellets; cells were incubated at 37 °C for 12 min followed by 25 min at 4 °C. Cells were washed with PBS, then stained with viability dye. After a wash, cells were stained with surface and intracellular markers as instructed below in the flow cytometry section.

To examine the viral load, kidneys were harvested, weighed, and homogenized Clarified homogenates were kept on ice. Vero cell monolayers were rinsed by inverting plates to discard medium. 200 µL of diluted tissue homogenates were added per well without touching the cell layer and gently rotated to distribute evenly. Absorption proceeded for 60 min at 37 °C with gentle shaking every 10 min. After the absorption stage, a total of 4 mL of the 1× agarose overlay was dispensed per well along the wall and plates were left at room temperature for ~10 min to solidify before returning to the incubator. Plates were incubated for 4 days at 37 °C with 5% CO2. On day 5, neutral red was prepared as a 1% aqueous solution and mixed 1:1 with 2× plaque assay medium. Each well received 1.5 mL of the neutral red overlay and was incubated overnight at 37 °C. Plaques were enumerated the following day (Day 6). PFU per gram of tissue were calculated by counting plaques at dilutions yielding 10–200 plaques, then multiplying by the dilution factor and normalizing to inoculum volume and tissue mass.

Spleen processing and T cell activation

Spleens were harvested from 8- to 16-week-old mice and mechanically dissociated in a 6-well plate containing 2 mL of red blood cell lysis buffer (ACK buffer). An additional 2 mL of lysis buffer was added, followed by a 5 min incubation at room temperature. The reaction was quenched with 20 mL of phosphate-buffered saline (PBS), and the suspension was filtered through a 70 µm cell strainer. Cells were pelleted by centrifugation at 350 × *g* for 5 min.

Splenocyte pellets were resuspended in 1 mL of FACS buffer (PBS supplemented with 2 mM EDTA and 2% fetal bovine serum [FBS]). Viable cells were quantified by Trypan blue exclusion using a Neubauer hemocytometer. CD3 + T cells were isolated via magnetic bead-based negative selection (StemCell Technologies). Following isolation, 2×10^6 T cells/mL were seeded in 1 mL of activation medium (RPMI-1640 with L-glutamine, 10% FBS, 1 M HEPES, and 0.1% β-mercaptoethanol) in a 48-well plate. Cells were activated with 1 µg/mL anti-CD3ε antibody (clone 145-2C11) for 24 h at 37 °C under standard culture conditions.

Anti-PD-1 antibodies (Leinco) and SB415286 (Selleckchem) were reconstituted at 1 mg/mL in sterile phosphate-buffered saline. Mice were administered 200 µg of the antibody solution via intraperitoneal injection every 48 h, starting on day 6 post-tumor implantation and continuing until tumor resection on day 16. The concentration of SB415286 for optimal specific effects and ita optimal frequency of use were based on previously reported studies.[42,56,58]

CD4 + , CD8, and CTLA-4 T-cell depletion

To deplete CD4 + T cells, mice received 300 µg of anti-CD4 antibody (Leinco) via intraperitoneal injection 24 hours prior to tumor implantation (day -1), with subsequent doses administered on days 7 and 14 post-implantation. This regimen ensured sustained depletion throughout the experimental timeline. The same regime was used in the depletion of Tregs with anti-CTLA-4. C57BL/6 mice were injected with 1×10^5 B16F10 melanoma cells. In the αCTLA4 groups, mice received 200 µg of CTLA4 (clone 9d9) blocking antibody (Leinco) IP at 4, 7, and 10 days thereafter. Tumors were measured by caliper every three days, and tumor volume was calculated as length x width x width/2. At the time of sacrifice for analysis, mice were euthanized using CO_2 and subsequent cervical dislocation. Similarly, to deplete CD8 + T cells, mice received 300 µg of anti-CD8 antibody (e.g., anti-mouse CD8 alpha clone 53-6.7 for mice) via intraperitoneal injection 24 h prior to tumor implantation (day -1), with subsequent doses administered on days 7 and 14 post-implantation. A non-specific IgG antibody of the same isotype as the anti-CD8 (the isotype control) is prepared at the same concentration and used as a control to account for non-specific effects of MAb administration. For the identification of tumor reactive TILs from B16 F10 tumors, we used H-2Kb TRP-2 BV421 tetramers (Mouse MHC Class 1; TRP-2 180-188 (SVYDFFVWL). TRP-2 (Tyrosinase-related protein 2) is a melanocyte differentiation antigen expressed by B16 melanoma cells.

Glucose uptake and metabolic profiling in activated T cells

Splenocytes were isolated and activated with 1 µg/mL anti-CD3ε antibody (clone 145-2C11) for 48 h at 37 °C under standard culture conditions. For glucose uptake assessment, activated cells were incubated with 2-NBDG (Thermo Fisher Scientific, #N13195) at a 1:1000 dilution in phosphate-buffered saline (PBS) for 1 h at 37 °C, followed by fluorescence quantification via flow cytometry.

Seahorse glycolysis and oxidated phosphorylation test

Oxygen consumption rate (OCR) and extracellular acidification rate (ECAR) were quantified using a Seahorse XFe96 Analyzer (Agilent Technologies). The day before the assay, 96-well Seahorse microplates were coated with poly-D-lysine (5 µg/mL) and

incubated overnight. Sensor cartridges were hydrated overnight in XF calibrant at 37 °C in a non-CO2 incubator. On the day of the assay, wells were rinsed and seeded with 1×10^6 T cells per well in XF RPMI assay medium (pH 7.4). For glycolysis stress tests, medium was supplemented with 2 mM L-glutamine. For mitochondrial stress tests, medium contained 2 mM L-glutamine, 25 mM D-glucose, and 2 mM sodium pyruvate. Plates were equilibrated for 1 h at 37 °C in a non-CO2 incubator prior to measurement.

Injection solutions were prepared according to the manufacturer's instructions and loaded into the designated ports of the hydrated sensor cartridge. For glycolysis assays, cells were sequentially injected with D-glucose (final 10 mM), oligomycin (final 5 µM), and 2-deoxy-D-glucose (final 100 mM). For mitochondrial stress tests, oligomycin (final 1.5 µM), FCCP (final 2 µM), and rotenone/antimycin A (final 0.5 µM each) were injected in sequence. OCR and ECAR were recorded using Wave software (Agilent Technologies) and normalized to cell number. MitoSpy™ Green FM staining was performed to quantify mitochondrial mass. Cells were incubated with MitoSpy Green FM (100 nM; BioLegend) for 30 min at 37 °C, washed with PBS, and immediately analyzed by flow cytometry. As the dye accumulates in mitochondria independently of membrane potential, it provides a reliable measure of total mitochondrial content.

SCENITH cellular metabolic assay

T cell metabolic activity at cellular level was quantified using the SCENITH assay, which measures protein synthesis as a readout of pathway-specific ATP dependence under acute metabolic inhibition, as described earlier.[79] Briefly, primary splenocytes were isolated and stimulated with anti-CD3 and anti-CD28, then exposed for 20 min at 37 °C to vehicle or metabolic inhibitors prepared in complete medium: 2-deoxy-D-glucose (2-DG, 100 mM) to block glycolysis, oligomycin (2 µM) to inhibit mitochondrial ATP synthase, or their combination (2-DG 100 mM + oligomycin 2 µM). Following the preincubation, ongoing translation was pulse-labeled with 50 µg/mL puromycin for 30 min at 37 °C. Cells were washed with cold PBS, stained for viability. Anti-puromycin antibody was added with the following surface markers for flow cytometry. Puromycin mean fluorescence intensity (MFI) in each inhibitor condition was used to compute glycolytic, mitochondrial, and glycolysis-independent contributions to ATP-supported protein synthesis, normalized to the vehicle control.

Cell preparation and immunophenotyping

Organs were harvested from 8- to 16-week-old mice. Inguinal lymph nodes (LN) and thymus were mechanically dissociated through a 70 µm cell strainer using the plunger of a 5 mL syringe. The strainer was washed with 5 mL of FACS buffer (PBS supplemented with 10 mM EDTA and 2% fetal bovine serum [FBS]). Tumors were mechanically disrupted on 70 µm strainers in RPMI medium on ice. Tumor lysates were centrifuged at $350 \times g$ for 5 min and resuspended in PBS. The tumor lysate in PBS was layered onto lymphocyte separation medium (Corning) and centrifuged at 2000 rpm for 20 min at room temperature to isolate tumor-infiltrating lymphocytes (TILs).

For cell blocking and staining, isolated cells from spleen, LN, thymus, and tumor were blocked with 100 µL of PBS containing 10 mM EDTA, 5% FBS, and 2.5 ng/mL purified rat anti-mouse CD16/CD32 (BD Biosciences #553141) for 20 min at 4 °C. Cells were then centrifuged at $350 \times g$ for 5 min and stained with primary antibodies (as detailed in the supplementary Table 1) for 30 min at 4 °C. Each staining mix was supplemented with 1/1000 Fixable Viability Dye eFluor™ 780. Following staining, cells were fixed with 2% paraformaldehyde (PAF) for 15 min at 4 °C, washed twice with PBS/10 mM EDTA + 2% FBS, and then permeabilized using the FoxP3/ Transcription Staining Buffer Set (eBioscience) for 30 min at 4 °C. Cells were stained with antibodies targeting intracellular proteins, diluted in permeabilization buffer, for 50 min at room temperature. After staining, cells were washed twice with PBS/ 10 mM EDTA + 2% FBS.

Flow cytometric analysis, cell suspensions were analyzed using a BD LSRFortessa flow cytometer. Mean fluorescence intensity (MFI) of specific markers was quantified on T cell subpopulations using FlowJo software (Tree Star, Ashland, USA). Results were further analyzed using FlowJo to assess immunophenotypic profilesv.

Regulatory T-cell suppression assay

To assess the suppressive capacity of regulatory T cells (Tregs), T_{reg} and T_{conv} cells were purified by magnetic cell sorting from splenocytes using EasySep Mouse $CD4^+$ $CD25^+$ Regulatory T cell isolation kit II (Stemcell technologies). T_{resp} cells were purified from WT mice as $CD4^+$ $CD25^-$ cells and labelled with Tagit Violet proliferation and cell tracking dye (Biolegend). $CD4^+$ $CD25^-$ T_{conv} cells were also isolated from GSK-3 KD mice to assess baseline differences in activation and proliferation between WT and GSK-3 KD cells. T_{reg} cells were purified as $CD4^+$ $CD25^+$ from either WT or GSK-3 KD mice and purity was confirmed by flow cytometry analysis of CD4 and Foxp3 expression at time zero. T_{reg} purity was superior to 80% and T_{resp} purity was superior to 98% for all data shown and there was no difference in purity between WT and GSK-3 KD samples. Feeder cells were obtained from total WT splenocytes and mitomycin-C inactivated (100 µg/ml) for 1 h at 37 °C. T_{reg} cells were co-cultured at various ratios (from 1:1 to 1:16) with T_{resp} cells (5×10^4), and accessory cells (1×10^5) in RPMI 1640 (Corning) supplemented with 10%FBS in the presence of soluble αCD3 (0.5 µg/mL, clone 2C11) for 72 h at 37 °C. Cells were then collected and stained for flow cytometry analysis of proliferation dye dilution and expression of additional activation markers. Following 72 h of activation, T_{resp} cells are subsequently defined as Live $Tagit^+$ $CD4^+$ $Foxp3^-$ and T_{reg} cells are defined as Live $Tagit^-$ $CD4^+$ $Foxp3^+$ cells and proliferation was assessed by dilution of the Tagit dye and quantified by division and proliferation indexes. % suppression was calculated by comparing division indexes using 0:1 as a baseline for the absence of Treg-mediated suppression.This system allows a direct measurement of Treg-mediated inhibition of conventional T-cell expansion in vitro.[116]

Immunoblotting

Cell lysates were prepared by resuspension of spleen-purified $CD8^+$ T cells in 1% Triton X-100 lysis buffer, followed by a 30 min incubation on ice as described.[117] Lysates were centrifuged at 14,000 rpm for 30 min at 4 °C and the nuclear-free supernatants were subjected to SDS-PAGE on a 10% polyacrylamide gel. Proteins from the gel were electroblotted onto nitrocellulose membranes at 100 V for 75 min, followed by 1 h of blocking with 3% BSA in TBST at RT. The nitrocellulose membranes were then incubated in the presence of the indicated primary Abs, followed by incubation with HRP-conjugated secondary Abs. Immunoreactive protein bands were visualized using an ECL reagent and autoradiography. Whenever required, nitrocellulose membranes were stripped by incubation in stripping buffer for 20 min at RT, followed by 1 h incubation with blocking buffer (3% BSA in TBST).

Mass cytometry (CyTOF)

Mass cytometry (CyTOF) analysis was performed at the McGill University CyTOF facility

following standardized protocols. Single-cell suspensions (3×10^6 cells) were stained with 5 µM Cell-ID™ Cisplatin (Fluidigm, San Francisco, CA) for viability assessment, followed by32quenching with MaxPar® Cell Staining Buffer at a 5:1 volume ratio. Following centrifugation (300 g, 5 min, 4 °C), cells were resuspended in 50 µL buffer and incubated with human Fc receptor blocking solution (5 µL; BioLegend, San Diego, CA) for 10 min at room temperature. Surface marker staining was performed using

50 µL of pre-titrated metal conjugated antibody cocktail for 30 min (detailed panel composition in ref..[20]) After washing, cellular DNA was labeled overnight at 4 °C using 1 mL intercalation solution containing 125 nM MaxPar® Intercalator-Ir in MaxPar® Fix and Perm Buffer. Prior to data acquisition, cells were washed with MaxPar® Water, resuspended with EQ™ Four Element Calibration Beads, and analyzed on a Helios™ CyTOF II mass cytometer. A minimum of 100,000 viable single cells were acquired per sample at an event rate of 300–500 events/second.

Mass cytometry data analysis

Mass cytometry data analysis was performed using the Cytobank platform (Cytobank Inc.,

Mountain View, CA) following previously established protocols94, 95. All samples underwent simultaneous normalization and analysis to minimize technical variation and account for signal drift during extended acquisition periods. A standardized high-level gating strategy was implemented across all CyTOF files, incorporating sequential gates for event length, bead exclusion, cell viability, and DNA content. For comprehensive analysis, individual sample files were concatenated into a single dataset, from which population-specific data were subsequently extracted and separated into individual files for comparative analyses. Dimensional reduction was performed using t-Distribution Stochastic Neighbor Embedding (tSNE) analysis, which generated a two-dimensional representation (tSNE1 versus tSNE2) of the high-dimensional data by preserving local phenotypic relationships between cells, enabling visualization and identification of distinct cell populations based on their marker expression profiles.

Sample preparation for RNAseq and RNA profiling

Tumor was prepared as previously described and CD8+ TILs were isolated (Stemcell Technologies) RNA was isolated using the miRNeasy Mini Kit (Qiagen), and the mRNA was purified from 1 ug of total RNA using the Dynabeads mRNA DIRECT Micro Kit (Thermo Fisher Scientific). The reverse transcription used SuperScript VILO cDNA Synthesis kit (Thermo Fisher Scientific). The whole transcriptome libraries were prepared using the Ion Total RNA-Seq Kit version 2 Kit (Thermo Fisher Scientific). The yield and size distribution of the amplified libraries were assessed with Agilent Bioanalyzer using Ion AmpliSeq transcriptome Mouse gene expression Kit (Thermo Fisher Scientific). Sequencing was performed on an Ion Proton Instrument (Ion Torrent, Thermo Fisher Scientific).

Bone marrow cultures with GM-CSF

Bone marrow cells, at a concentration of 10^6 cells per well, were seeded into 6-well tissue culture plates, each containing 4 ml of medium consisting of RPMI 1640, supplemented with glutamine, penicillin, streptomycin, 2-mercaptoethanol (all from Invitrogen), 10% heat-inactivated fetal calf serum and GM-CSF at 20 ng/ml (Peprotech) according to Helft et al 2015.[118] This culture was incubated at various days to generate a dendritic cell enriched population. On day 2, 2 ml of the existing medium was removed and replaced with 2 ml of fresh media with GM-CSF. On day 3, all medium was replaced with 4 ml of fresh medium containing 20 ng/ml GM-CSF. In some experiments, IL-4 (Peprotech) was added to the medium at a concentration of 5 ng/ml, along with GM-CSF. On day 6-8, non-adherent cells from the culture supernatant and the loosely adherent cells were harvested by gentle washing with PBS, were collected and combined.

Bioinformatics

Bulk RNA-seq of libraries prepared from B16-F10 tumor-infiltrating T cells was performed at the Institute for Research in Immunology and Cancer (IRIC), Université de Montréal. RNA-sequencing (RNA-seq) analysis was done using the Torrent Suite software version 5.4.0 and the RNA Seq Analysis plugin (Thermo Fisher Scientific) on the mouse reference genome mm10 using STAR. Gene level expression is calculated using HTSeq and Picard to report raw read counts and FPKM (fragment per kilobase of transcript per million).[119] Differential gene expression was analyzed with DESeq2.[120] Differential expression results were visualized with the R package ggplot2.[121] Downstream pathway analysis was conducted using Gene Set Enrichment Analysis (GSEA).[122] Cytoscape and the String application were employed to extract and visualize known interactions which used for the downstream Gene Ontology.[123,124]

Statistical analysis

Respect for the assumptions of normal distribution of residuals and homoscedasticity was verified, and data were presented as mean + SEM as well as individual values, unless otherwise indicated. Data from independent experiments were pooled for analysis in each data panel, unless otherwise indicated. Statistical analyses were performed using Prism 8 (GraphPad Software). One-/two-way ANOVA was performed unless otherwise indicated in the figure legends. We considered a P-value lower than 0,05 as significant. N.S.: $P > 0,05$; *: $P < 0,05$; **: $P < 0,01$; ***: $P < 0,001$; ****$P < 0,0001$.

Animal experiment ethical approval

The authors respect ethical guidelines for animal welfare. All mice were housed in the Maisonneuve–Rosemont Hospital Research Centre (CRHMR) animal facility (containment level 2 for LCMV experiments) under a 12-hour light–dark cycle with ad libitum access to food and water. The animal care program is accredited with the Certificate of Good Animal Practice (GAP) issued by the Canadian Council on Animal Care (CCAC). All experiments involved in the use of animals were approved, reviewed, and overseen by the institutional Committee for the Protection of Animals (CPA). The following approved protocols were used: in-house breeding (2021-2537); use of primary cells for ex vivo studies (2024-3547); LCMV Clone 13 and Armstrong infections (2023-3032); and inoculation of B16 melanomas with relevant treatments (2025-3941).

MATERIALS AVAILABILITY

A complete list of the reagents and antibodies used in this manuscript can be found in supplementary table S1.

DATA AVAILABILITY

The raw sequence data reported in this paper have been deposited in the Genome Sequence Archive in National Genomics Data Center, China National Center for Bioinformation / Beijing Institute of Genomics, Chinese Academy of Sciences (GSA: CRA039207) that are publicly accessible at https://ngdc.cncb.ac.cn/gsa.

ACKNOWLEDGEMENTS

We thank Dale Iong and his team from NIH Tetramer Core Facility at Emory for providing GP33 tetramers and Frederic Duval and Anne-Marie Aubin from the Flow Cytometry Core Facility of CR-HMR for their help. We thank Dr. Vinicius Motta and the McGill University CyTOF core facility for technical support with CyTOF data acquisition and analysis. We also thank Ammar Sleitin and Drs. Mark Issa, Xueyang Guo and Virginie Calderon (IRCM) for helpful suggestions and discussions. This project was supported by the Canadian Institutes of Health Research Foundation grant (159912) (PI) and National Institutes of Health grant RO1 AI049466 (co-PI). C.E.R. is a founder and majority shareholder of ImmunAb Research Inc. (ImmunAb Recherche, Canada). All authors have read and approved the article.

AUTHOR CONTRIBUTIONS

B.M., H.T., C.L., M.A., and C.E.R. designed the study. B.M., J.K., A.K., C.L., N.P.A., L.C.P., L.H., A.L.C., A.N., M.A., and H.T. performed experiments. B.M., H.T., C.L., J.K., and A.K. analysed the data. B.M., H.T., C.L., M.A., and C.E.R. prepared figures. B.M. and C.E.R.

primarily wrote the manuscript. All authors discussed the data and reviewed the manuscript before submission. All authors read and approved the final manuscript. C.E.R. coordinated ethical approval to work with samples at the HMR.

ADDITIONAL INFORMATION

Supplementary information The online version contains supplementary material available at https://doi.org/10.1038/s41392-026-02663-y.

Competing interests: C.E.R has received consulting fees from Freshfields Bruckhaus Deringer LLP (UK), Bristows LLP (UK), Proskauer Rose LLP (US) for patent consultancy work and is the founder of ImmunAb Res Inc (Canada) with patents relating to immunotherapies. The other authors declare no competing interests.

Animal ethics approval: Animal experiments were approved by the Animal Care Use and Review Committee of Center Research -Hospital Maisonneuve Rosemont (CR-HMR) (ethical approval no 2021-2516, 2023-3032 and 2024-3547) from University of Montreal. For mouse tumor experiments, all tumor sizes/burdens were permitted by the CR-HMR of Montreal University. Maximal tumor burden permitted by the CR-HMR (1.5 cm3) was not exceeded in this study.

Publisher's note Springer Nature remains neutral with regard to jurisdictional claims in published maps and institutional affiliations.

REFERENCES

1. Kalia, V., Sarkar, S. & Ahmed, R. Fine-tuning CD4+ central memory T cell heterogeneity by strength of stimulation. *Eur. J. Immunol.* **38**, 15–19 (2008).
2. Topchyan, P., Lin, S. & Cui, W. The role of CD4 T cell help in CD8 T cell differentiation and function during chronic infection and cancer. *Immune Netw.* **23**, e41 (2023).
3. Laidlaw, B. J., Craft, J. E. & Kaech, S. M. The multifaceted role of CD4(+) T cells in CD8(+) T cell memory. *Nat. Rev. Immunol.* **16**, 102–111 (2016).
4. Aubert, R. D. et al. Antigen-specific CD4 T-cell help rescues exhausted CD8 T cells during chronic viral infection. *Proc. Natl. Acad. Sci. USA* **108**, 21182–21187 (2011).
5. Battegay, M. et al. Enhanced establishment of a virus carrier state in adult CD4+ T-cell-deficient mice. *J. Virol.* **68**, 4700–4704 (1994).
6. Borst, J., Ahrends, T., Babala, N., Melief, C. J. M. & Kastenmuller, W. CD4(+) T cell help in cancer immunology and immunotherapy. *Nat. Rev. Immunol.* **18**, 635–647 (2018).
7. Zajac, A. J. et al. Viral immune evasion due to persistence of activated T cells without effector function. *J. Exp. Med.* **188**, 2205–2213 (1998).
8. Oh, D. Y. et al. Intratumoral CD4(+) T cells mediate anti-tumor cytotoxicity in human bladder cancer. *Cell* **181**, 1612–1625 (2020).
9. Mikami, N. & Sakaguchi, S. Regulatory T cells in autoimmune kidney diseases and transplantation. *Nat. Rev. Nephrol.* **19**, 544–557 (2023).
10. Tay, C., Tanaka, A. & Sakaguchi, S. Tumor-infiltrating regulatory T cells as targets of cancer immunotherapy. *Cancer Cell* **41**, 450–465 (2023).
11. Wood, K. J. & Sakaguchi, S. Regulatory T cells in transplantation tolerance. *Nat. Rev. Immunol.* **3**, 199–210 (2003).
12. McLane, L. M., Abdel-Hakeem, M. S. & Wherry, E. J. CD8 T cell exhaustion during chronic viral infection and cancer. *Annu. Rev. Immunol.* **37**, 457–495 (2019).
13. Hudson, W. H. et al. Proliferating transitory T cells with an effector-like transcriptional signature emerge from PD-1(+) stem-like CD8(+) T cells during chronic infection. *Immunity* **51**, 1043–1058 (2019).
14. Chen, Z. et al. TCF-1-centered transcriptional network drives an effector versus exhausted CD8 T cell-fate decision. *Immunity* **51**, 840–855 e845 (2019).
15. Baumeister, S. H., Freeman, G. J., Dranoff, G. & Sharpe, A. H. Coinhibitory pathways in immunotherapy for cancer. *Annu Rev. Immunol.* **34**, 539–573 (2016).
16. Lin, W. W. et al. CD8(+) T lymphocyte self-renewal during effector cell determination. *Cell Rep.* **17**, 1773–1782 (2016).
17. Pais Ferreira, D. et al. Central memory CD8(+) T cells derive from stem-like Tcf7(hi) effector cells in the absence of cytotoxic differentiation. *Immunity* **53**, 985–1000 (2020).
18. Gullicksrud, J. A. et al. Differential requirements for Tcf1 long isoforms in CD8(+) and CD4(+) T cell responses to acute viral infection. *J. Immunol.* **199**, 911–919 (2017).
19. Lin, W. H. et al. Asymmetric PI3K signaling driving developmental and regenerative cell fate bifurcation. *Cell Rep.* **13**, 2203–2218 (2015).
20. Sharma, P. et al. The next decade of immune checkpoint therapy. *Cancer Discov.* **11**, 838–857 (2021).
21. Chamoto, K., Yaguchi, T., Tajima, M. & Honjo, T. Insights from a 30-year journey: function, regulation and therapeutic modulation of PD1. *Nat. Rev. Immunol.* **23**, 682–695 (2023).
22. Sharma, A. et al. Anti-CTLA-4 immunotherapy does not deplete FOXP3(+) regulatory T cells (Tregs) in human cancers-response. *Clin. Cancer Res.* **25**, 3469–3470 (2019).
23. Leach, D. R., Krummel, M. F. & Allison, J. P. Enhancement of antitumor immunity by CTLA-4 blockade. *Science* **271**, 1734–1736 (1996).
24. Ott, P. A., Hodi, F. S. & Robert, C. CTLA-4 and PD-1/PD-L1 blockade: new immunotherapeutic modalities with durable clinical benefit in melanoma patients. *Clin. Cancer Res.* **19**, 5300–5309 (2013).
25. Ben Saad, E., Oroya, A., Anto, N. P., Bachais, M. & Rudd, C. E. PD-1 endocytosis unleashes the cytolytic potential of checkpoint blockade in tumor immunity. *Cell Rep.* **43**, 114907 (2024).
26. Siddiqui, I. et al. Intratumoral TCF1(+)PD-1(+)CD8(+) T cells with stem-like properties promote tumor control in response to vaccination and checkpoint blockade immunotherapy. *Immunity* **50**, 195–211 (2019).
27. Sade-Feldman, M. et al. Resistance to checkpoint blockade therapy through inactivation of antigen presentation. *Nat. Commun.* **8**, 1136 (2017).
28. Miller, B. C. et al. Subsets of exhausted CD8(+) T cells differentially mediate tumor control and respond to checkpoint blockade. *Nat. Immunol.* **20**, 326–336 (2019).
29. Barry, M. & Bleackley, R. C. Cytotoxic T lymphocytes: all roads lead to death. *Nat. Rev. Immunol.* **2**, 401–409 (2002).
30. Cullen, S. P., Brunet, M. & Martin, S. J. Granzymes in cancer and immunity. *Cell Death Differ.* **17**, 616–623 (2010).
31. Hay, Z. L. Z. et al. Granzyme F: exhaustion marker and modulator of chimeric antigen receptor T cell-mediated cytotoxicity. *J. Immunol.* **212**, 1381–1391 (2024).
32. Johnson, H., Scorrano, L., Korsmeyer, S. J. & Ley, T. J. Cell death induced by granzyme C. *Blood* **101**, 3093–3101 (2003).
33. Rudd, C. E. How the discovery of the CD4/CD8-p56(LCK) complexes changed immunology and immunotherapy. *Front. Cell Dev. Biol.* **9**, 626095 (2021).
34. Samelson, L. E. Signal transduction mediated by the T cell antigen receptor: the role of adapter proteins. *Annu Rev. Immunol.* **20**, 371–394 (2002).
35. Cantrell, D. Signaling in lymphocyte activation. *Cold Spring Harb. Perspect. Biol.* **7**, a018788 (2015).
36. Rudd, C. E. Adaptors and molecular scaffolds in immune cell signaling. *Cell* **96**, 5–8 (1999).
37. Courtney, A. H. et al. CD45 functions as a signaling gatekeeper in T cells. *Sci. Signal* **12** (2019).
38. Barber, E. K., Dasgupta, J. D., Schlossman, S. F., Trevillyan, J. M. & Rudd, C. E. The CD4 and CD8 antigens are coupled to a protein-tyrosine kinase (p56lck) that phosphorylates the CD3 complex. *Proc. Natl. Acad. Sci. USA* **86**, 3277–3281 (1989).
39. Wei, Q. et al. LCK bound to coreceptor is less active than free LCK. *Proc. Natl. Acad. Sci. USA* **117**, 15809–15817 (2020).
40. Chan, A. C., Iwashima, M., Turck, C. W. & Weiss, A. ZAP-70: a 70 kd protein-tyrosine kinase that associates with the TCR zeta chain. *Cell* **71**, 649–662 (1992).
41. Sharma, S. et al. An siRNA screen for NFAT activation identifies septins as coordinators of store-operated Ca2+ entry. *Nature* **499**, 238–242 (2013).
42. Taylor, A. et al. Glycogen synthase kinase 3 inactivation drives T-bet-mediated downregulation of co-receptor PD-1 to enhance CD8(+) cytolytic T cell responses. *Immunity* **44**, 274–286 (2016).
43. Woodgett, J. R. Molecular cloning and expression of glycogen synthase kinase-3/factor A. *EMBO J.* **9**, 2431–2438 (1990).
44. Doble, B. W. & Woodgett, J. R. GSK-3: tricks of the trade for a multi-tasking kinase. *J. Cell Sci.* **116**, 1175–1186 (2003).
45. Rayasam, G. V., Tulasi, V. K., Sodhi, R., Davis, J. A. & Ray, A. Glycogen synthase kinase 3: more than a namesake. *Br. J. Pharm.* **156**, 885–898 (2009).
46. Frame, S. & Cohen, P. GSK3 takes centre stage more than 20 years after its discovery. *Biochem. J.* **359**, 1–16 (2001).
47. Hughes, K., Nikolakaki, E., Plyte, S. E., Totty, N. F. & Woodgett, J. R. Modulation of the glycogen synthase kinase-3 family by tyrosine phosphorylation. *Embo J.* **12**, 803–808 (1993).
48. Eldar-Finkelman, H. & Martinez, A. GSK-3 inhibitors: preclinical and focus on CNS. *Front. Mol. Neurosci.* https://doi.org/10.3389/fnmol.2011.00032 (2011).
49. Ohteki, T. et al. Negative regulation of T cell proliferation and interleukin 2 production by the serine threonine kinase GSK-3. *J. Exp. Med.* **192**, 99–104 (2000).
50. Zhang, B., Feng, H., Lin, H. & Li, R. Somatostatin-SSTR3-GSK3 modulates human T-cell responses by inhibiting OXPHOS. *Front. Immunol.* **15**, 1322670 (2024).
51. Cichocki, F. et al. GSK3 inhibition drives maturation of NK cells and enhances their antitumor activity. *Cancer Res.* **77**, 5664–5675 (2017).
52. Embi, N., Rylatt, D. B. & Cohen, P. Glycogen synthase kinase-3 from rabbit skeletal muscle. Separation from cyclic-AMP-dependent protein kinase and phosphorylase kinase. *Eur. J. Biochem. FEBS* **107**, 519–527 (1980).
53. Beurel, E., Grieco, S. F. & Jope, R. S. Glycogen synthase kinase-3 (GSK3): regulation, actions, and diseases. *Pharm. Ther.* **148**, 114–131 (2015).

54. Gounari, F. & Khazaie, K. TCF-1: a maverick in T cell development and function. *Nat. Immunol.* **23**, 671–678 (2022).
55. Zhao, P., Sun, L. & Zhao, C. TCF1/LEF1 triggers WNT-dependent chemokine/cytokine-induced inflammation and cadherin pathways to drive T-ALL cell migration. *Biochem. Biophys. Rep.* **34**, 101457 (2023).
56. Taylor, A. & Rudd, C. E. Glycogen synthase kinase 3 (GSK-3) controls T-cell motility and interactions with antigen presenting cells. *BMC Res. Notes* **13**, 163 (2020).
57. Rudd, C. E., Chanthong, K. & Taylor, A. Small molecule inhibition of GSK-3 specifically inhibits the transcription of inhibitory co-receptor LAG-3 for enhanced anti-tumor immunity. *Cell Rep.* **30**, 2075–2082 (2020).
58. Taylor, A., Rothstein, D. & Rudd, C. E. Small-molecule inhibition of PD-1 transcription Is an effective alternative to antibody blockade in cancer therapy. *Cancer Res.* **78**, 706–717 (2018).
59. Krueger, J. & Rudd, C. E. Two strings in one bow: PD-1 negatively regulates via co-receptor CD28 on T cells. *Immunity* **46**, 529–531 (2017).
60. Steele, L. et al. Non-redundant activity of GSK-3alpha and GSK-3beta in T cell-mediated tumor rejection. *iScience* **24**, 102555 (2021).
61. Taylor, A. & Rudd, C. E. Glycogen synthase kinase 3 inactivation compensates for the lack of CD28 in the priming of CD8(+) cytotoxic T-cells: implications for anti-PD-1 immunotherapy. *Front. Immunol.* **8**, 1653 (2017).
62. Huntington, K. E. et al. GSK-3 inhibitor Elraglusib enhances tumor-infiltrating immune cell activation in tumor biopsies and synergizes with anti-PD-L1 in a murine model of colorectal cancer. *Int. J. Mol. Sci.* **24**, 10870 (2023).
63. Shaw, G., Cavalcante, L., Giles, F. J. & Taylor, A. Elraglusib (9-ING-41), a selective small-molecule inhibitor of glycogen synthase kinase-3 beta, reduces expression of immune checkpoint molecules PD-1, TIGIT and LAG-3 and enhances CD8(+) T cell cytolytic killing of melanoma cells. *J. Hematol. Oncol.* **15**, 134 (2022).
64. Van Oers, N. S. et al. Disruption of CD8-dependent negative and positive selection of thymocytes is correlated with a decreased association between CD8 and the protein tyrosine kinase, p56lck. *Eur. J. Immunol.* **22**, 735–743 (1992).
65. Barber, D. L. et al. Restoring function in exhausted CD8 T cells during chronic viral infection. *Nature* **439**, 682–687 (2006).
66. Herndler-Brandstetter, D. et al. KLRG1(+) effector CD8(+) T cells lose KLRG1, differentiate into all memory T cell lineages, and convey enhanced protective immunity. *Immunity* **48**, 716–729 (2018).
67. Gill, A. L. et al. PD-1 blockade increases the self-renewal of stem-like CD8 T cells to compensate for their accelerated differentiation into effectors. *Sci. Immunol.* **8**, eadg0539 (2023).
68. Im, S. J. et al. Defining CD8+ T cells that provide the proliferative burst after PD-1 therapy. *Nature* **537**, 417–421 (2016).
69. Kim, H. D. et al. Implication of CD69(+) CD103(+) tissue-resident-like CD8(+) T cells as a potential immunotherapeutic target for cholangiocarcinoma. *Liver Int.* **41**, 764–776 (2021).
70. Wherry, E. J. T cell exhaustion. *Nat. Immunol.* **12**, 492–499 (2011).
71. Abadie, K. et al. Reversible, tunable epigenetic silencing of TCF1 generates flexibility in the T cell memory decision. *Immunity* **57**, 271–286 (2024).
72. Xu, K. et al. Glycolysis fuels phosphoinositide 3-kinase signaling to bolster T cell immunity. *Science* **371**, 405–410 (2021).
73. Wu, M. et al. Glucose metabolism and function of CD4(+) tregs are regulated by the TLR8/mTOR signal in an environment of SKOV3 cell growth. *Cancer Med.* **12**, 16310–16322 (2023).
74. Sicheng F. et al. Immunometabolism regulates TCR recycling and iNKT cell functions. *Sci. Signal* **12**, eaau1778 (2019).
75. Palmer, C. S. et al. Regulators of glucose metabolism in CD4(+) and CD8(+) T cells. *Int. Rev. Immunol.* **35**, 477–488 (2016).
76. Frauwirth, K. A. et al. The CD28 signaling pathway regulates glucose metabolism. *Immunity* **16**, 769–777 (2002).
77. Macintyre, A. N. et al. The glucose transporter Glut1 is selectively essential for CD4 T cell activation and effector function. *Cell Metab.* **20**, 61–72 (2014).
78. Gantt, K. R. et al. The regulation of glucose transporter (GLUT1) expression by the RNA binding protein HuR. *J. Cell Biochem.* **99**, 565–574 (2006).
79. Argüello, R. J. et al. SCENITH: a flow cytometry-based method to functionally profile energy metabolism with single-cell resolution. *Cell Metab.* **32**, 1063–1075 (2020).
80. Sakaguchi, S., Yamaguchi, T., Nomura, T. & Ono, M. Regulatory T cells and immune tolerance. *Cell* **133**, 775–787 (2008).
81. Allard, D., Chrobak, P., Allard, B., Messaoudi, N. & Stagg, J. Targeting the CD73-adenosine axis in immuno-oncology. *Immunol. Lett.* **205**, 31–39 (2019).
82. Wei, S. C. et al. Distinct cellular mechanisms underlie anti-CTLA-4 and anti-PD-1 checkpoint blockade. *Cell* **170**, 1120–1133 (2017).
83. Gomez-Rodriguez, J., Kraus, Z. J. & Schwartzberg, P. L. Tec family kinases Itk and Rlk / Txk in T lymphocytes: cross-regulation of cytokine production and T-cell fates. *FEBS J.* **278**, 1980–1989 (2011).
84. Das, A. et al. Transcription factor Tox2 is required for metabolic adaptation and tissue residency of ILC3 in the gut. *Immunity* **57**, 1019–1036 (2024).
85. Russell, J. H. & Ley, T. J. Lymphocyte-mediated cytotoxicity. *Annu. Rev. Immunol.* **20**, 323–370 (2002).
86. Osinska, I., Popko, K. & Demkow, U. Perforin: an important player in immune response. *Cent. Eur. J. Immunol.* **39**, 109–115 (2014).
87. Jenne, D. et al. Identification and sequencing of cDNA clones encoding the granule-associated serine proteases granzymes D, E, and F of cytolytic T lymphocytes. *Proc. Natl. Acad. Sci. USA* **85**, 4814–4818 (1988).
88. Xin, C., Liu, P., Zhan, Q. & Cao, W. Gzmk(+) CD8 T cells in inflammatory diseases. *Front. Immunol.* **16**, 1661755 (2025).
89. Donado, C. A. et al. Granzyme K activates the entire complement cascade. *Nature* **641**, 211–221 (2025).
90. Shi, L., Wu, L., Wang, S. & Fan, Z. Granzyme F induces a novel death pathway characterized by Bid-independent cytochrome c release without caspase activation. *Cell Death Differ.* **16**, 1694–1706 (2009).
91. Nixon, B. G. et al. Cytotoxic granzyme C-expressing ILC1s contribute to antitumor immunity and neonatal autoimmunity. *Sci. Immunol.* **7**, eabi8642 (2022).
92. Harari, A., Bellutti Enders, F., Cellerai, C., Bart, P. A. & Pantaleo, G. Distinct profiles of cytotoxic granules in memory CD8 T cells correlate with function, differentiation stage, and antigen exposure. *J. Virol.* **83**, 2862–2871 (2009).
93. Kurschus, F. C. & Jenne, D. E. Delivery and therapeutic potential of human granzyme B. *Immunol. Rev.* **235**, 159–171 (2010).
94. Vick, S. C., Kolupaev, O. V., Perou, C. M. & Serody, J. S. Anti-PD-1 Checkpoint Therapy Can Promote the Function and Survival of Regulatory T Cells. *J. Immunol.* **207**, 2598–2607 (2021).
95. Kamada, T. et al. PD-1(+) regulatory T cells amplified by PD-1 blockade promote hyperprogression of cancer. *Proc. Natl. Acad. Sci. USA* **116**, 9999–10008 (2019).
96. Woods, D. M. et al. Decreased suppression and increased phosphorylated STAT3 in regulatory T cells are associated with benefit from adjuvant PD-1 blockade in resected metastatic melanoma. *Clin. Cancer Res.* **24**, 6236–6247 (2018).
97. Dodagatta-Marri, E. et al. alpha-PD-1 therapy elevates Treg/Th balance and increases tumor cell pSmad3 that are both targeted by alpha-TGFbeta antibody to promote durable rejection and immunity in squamous cell carcinomas. *J. Immunother. Cancer* **7**, 62 (2019).
98. Utzschneider, D. T. et al. T cell factor 1-expressing memory-like CD8(+) T cells sustain the immune response to chronic viral infections. *Immunity* **45**, 415–427 (2016).
99. Jadhav, R. R. et al. Epigenetic signature of PD-1+ TCF1+ CD8 T cells that act as resource cells during chronic viral infection and respond to PD-1 blockade. *Proc. Natl. Acad. Sci. USA* **116**, 14113–14118 (2019).
100. Tu, T. H. et al. Decreased progenitor TCF1 + T-cells correlate with COVID-19 disease severity. *Commun. Biol.* **7**, 526 (2024).
101. Buck, M. D., Sowell, R. T., Kaech, S. M. & Pearce, E. L. Metabolic Instruction of Immunity. *Cell* **169**, 570–586 (2017).
102. O'Sullivan, D. & Pearce, E. L. Targeting T cell metabolism for therapy. *Trends Immunol.* **36**, 71–80 (2015).
103. Pearce, E. L., Poffenberger, M. C., Chang, C. H. & Jones, R. G. Fueling immunity: insights into metabolism and lymphocyte function. *Science* **342**, 1242454 (2013).
104. Bengsch, B. et al. Bioenergetic insufficiencies due to metabolic alterations regulated by the inhibitory receptor PD-1 are an early driver of CD8(+) T cell exhaustion. *Immunity* **45**, 358–373 (2016).
105. Schurich, A. et al. Distinct metabolic requirements of exhausted and functional virus-specific CD8 T cells in the same host. *Cell Rep.* **16**, 1243–1252 (2016).
106. Theeuwes, W. F. et al. Inactivation of glycogen synthase kinase-3beta (GSK-3beta) enhances skeletal muscle oxidative metabolism. *Biochim. Biophys. Acta Mol. Basis Dis.* **1863**, 3075–3086 (2017).
107. Ivanova, M. E. et al. The pore conformation of lymphocyte perforin. *Sci. Adv.* **8**, eabk3147 (2022).
108. Kandasamy, M. et al. Glycogen synthase kinase-3 is essential for T(reg) development and function. *Cell Rep.* **44**, 116256 (2025).
109. Ye, Z. et al. The GSK3beta-beta-catenin-TCF1 pathway improves naive T cell activation in old adults by upregulating miR-181a. *npj Aging Mech. Dis.* **7**, 4 (2021).
110. Fu, Y. et al. Glycogen synthase kinase 3 controls T-cell exhaustion by regulating NFAT activation. *Cell Mol. Immunol.* **20**, 1127–1139 (2023).
111. Moes, B. & Rudd, C. E. Comment on: glycogen synthase kinase 3 controls T-cell exhaustion by regulating NFAT activation. *Cell Mol. Immunol.* **20**, 1127–1139 (2025).
112. Cao, X. et al. Granzyme B and perforin are important for regulatory T cell-mediated suppression of tumor clearance. *Immunity* **27**, 635–646 (2007).
113. Krueger, J., Rudd, C. E. & Taylor, A. Glycogen synthase 3 (GSK-3) regulation of PD-1 expression and and its therapeutic implications. *Semin Immunol.* **42**, 101295 (2019).
114. Sengupta, S., Katz, S. C., Sengupta, S. & Sampath, P. Glycogen synthase kinase 3 inhibition lowers PD-1 expression, promotes long-term survival and memory generation in antigen-specific CAR-T cells. *Cancer Lett.* **433**, 131–139 (2018).
115. Crespo, A. R., Luna, S. G., Moes, B., Rodriguez, A. & Rudd, C. E. The many faceted role of glycogen synthase kinase-3 (GSK-3) in T cells and cancer immunotherapy. *J. Cancer Biol.* **5**, 11–16 (2024).

116. Attias, M., Al-Aubodah, T. & Piccirillo, C. A. Mechanisms of human FoxP3(+) T(reg) cell development and function in health and disease. *Clin. Exp. Immunol.* **197**, 36–51 (2019).
117. Raab, M., da Silva, A. J., Findell, P. R. & Rudd, C. E. Regulation of Vav-SLP-76 binding by ZAP-70 and its relevance to TCR zeta/CD3 induction of interleukin-2. *Immunity* **6**, 155–164 (1997).
118. Helft, J. et al. GM-CSF mouse bone marrow cultures comprise a heterogeneous population of CD11c(+)MHCII(+) macrophages and dendritic cells. *Immunity* **42**, 1197–1211 (2015).
119. Anders, S., Pyl, P. T. & Huber, W. HTSeq—a Python framework to work with high-throughput sequencing data. *Bioinformatics* **31**, 166–169 (2015).
120. Love, M. I., Huber, W. & Anders, S. Moderated estimation of fold change and dispersion for RNA-seq data with DESeq2. *Genome Biol.* **15**, 550 (2014).
121. Wickham, H. GGplot2: elegant graphics for data analysis. https://ggplot2.tidyverse.org (Springer, 2016).
122. Subramanian, A. et al. Gene set enrichment analysis: a knowledge-based approach for interpreting genome-wide expression profiles. *Proc. Natl. Acad. Sci. USA* **102**, 15545–15550 (2005).
123. Doncheva, N. T., Morris, J. H., Gorodkin, J. & Jensen, L. J. Cytoscape StringApp: network analysis and visualization of proteomics data. *J. Proteome Res.* **18**, 623–632 (2019).
124. Ashburner, M. et al. Gene ontology: tool for the unification of biology. the gene ontology consortium. *Nat. Genet.* **25**, 25–29 (2000).

Open Access This article is licensed under a Creative Commons Attribution-NonCommercial-NoDerivatives 4.0 International License, which permits any non-commercial use, sharing, distribution and reproduction in any medium or format, as long as you give appropriate credit to the original author(s) and the source, provide a link to the Creative Commons licence, and indicate if you modified the licensed material. You do not have permission under this licence to share adapted material derived from this article or parts of it. The images or other third party material in this article are included in the article's Creative Commons licence, unless indicated otherwise in a credit line to the material. If material is not included in the article's Creative Commons licence and your intended use is not permitted by statutory regulation or exceeds the permitted use, you will need to obtain permission directly from the copyright holder. To view a copy of this licence, visit http://creativecommons.org/licenses/by-nc-nd/4.0/.

© The Author(s) 2026